Design, Fabrication and Characterization of Ultrasound Transducers for Fragmenting Large Renal Calculi

Akshay P. Randad

A thesis

submitted in partial fulfillment of the

requirements for the degree of

Master of Science in Mechanical Engineering

University of Washington

2018

Committee:

Michael R. Bailey

Adam D. Maxwell

Alberto Aliseda

Program Authorized to Offer Degree:

Department of Mechanical Engineering

University of Washington

Abstract

Design, Fabrication and Characterization of Ultrasound Transducers for Fragmenting Large Renal Calculi

Akshay P. Randad

Chair of the Supervisory committee:

Michael R. Bailey

Department of Mechanical Engineering

One in 11 people is affected by renal calculi (kidney stones) at some point in their life. There are different stone management techniques, but all have associated injuries to kidney or ureter and complications. Burst wave lithotripsy (BWL), developed recently by the Center for Industrial and Medical Ultrasound, has shown promising results for fragmenting stone non-invasively. BWL targets a stone with a series of pulses of small pressure amplitude at regular intervals of time to break the stone while minimizing tissue damage. BWL is still under development and its parameters need to be optimized. One of the challenges of BWL is to develop a transducer that

can fragment stones larger than 6 mm. The objective of this work was to develop a transducer that fragmented stones up to 12 mm. This was achieved by using piezoceramic materials that produced sufficient power for the fragmentation of large stones. Acoustic beam patterns were optimized using an iterative angular spectrum approach and rapid prototyped acoustic lenses. Finally, a BWL transducer was designed, fabricated and characterized to confirm the required outputs. The new transducer was demonstrated to fragment 11 mm stones 2.8 times more effectively than existing BWL transducers.

Table of Contents

Acknowledgement

I wish to thank my advisor and committee members: Prof. Michael R. Bailey, Prof. Adam D. Maxwell and Prof. Alberto Aliseda for the opportunity, guidance and support throughout the project. I would like to thank Mohamed A. Ghanem for his contribution in writing programs for implementing acoustic holography algorithm and allowing me to use one of his simulations of complex pressure profile. I wish to acknowledge Dr. Wayne Kreider, Ekaterina Kuznetsova, Brian MacConaghy, Bryan Cunitz, Christopher Hunter, Barbrina Dunmire, Dr. Dan Leotta, Dr. Christopher Bawiec, Dr. John Kucewicz and Prof. Oleg Sapozhnikov for their technical assistance in completing the project. I am thankful to all the members of Center for Industrial and Medical Ultrasound and Department of Urology who established facilities required for completing the project successfully. I want to thank Dr. Mathew Sorensen, Dr. Jonathan Harper and Dr. Justin Ahn for their insights from a medical perspective. Finally, I wish to give special thanks to my parents, friends and all the teachers I had until now for their guidance and support.

1 Introduction

Kidney stones currently affect 1 in 11 Americans over their lifetime[1] and the prevalence is rising. Although often asymptomatic in the kidney, a stone can cause debilitating pain, nausea, and/or difficulties in urination as it obstructs urine flow in the passage from the kidney to the bladder. If stones do not pass naturally (usually occurring when the size is >5 mm), at least one surgery must be performed to remove the stone. Once a patient has had a kidney stone, there is a 40% chance of having another symptomatic stone within 5 years [2]. Emergency room visits coupled with the various management options and monitoring for kidney stones have led to estimated annual costs in the United States of over $10 billion [3]. To reduce this burden on healthcare, efforts are being put in studying prevention techniques as well as alternative cost-effective therapeutic treatments for large stones. One of the ways to reduce cost of the surgery is to prevent complications through use of noninvasive or minimally invasive technologies for stone treatment. This chapter discusses various noninvasive therapeutic ultrasound technologies for stone management and their state of the art. First, a common noninvasive clinical treatment for stones called shock wave lithotripsy (SWL) and its physics, limitations and effects on body are discussed. Second, a new experimental technology called burst wave lithotripsy (BWL) is discussed. BWL attempts to address the limitations of SWL. Finally, we will conclude with the state of the art of BWL and its challenges.

1.1 Background

Human kidneys process one liter of blood every minute. They remove metabolic waste and water to form urine. In normal kidneys, microscopic crystals form in supersaturated urine and are passed

out of body harmlessly. If these crystals are not passed out and adhere to structures in kidney, they start to form stones (renal calculi). The most common type of kidney stone is calcium oxalate monohydrate or dihydrate (COM or COD). They account for nearly 80% of the stones in adults in the United States [2]. Other types of the stones are calcium phosphate, uric acid, struvite, and cystine. It is not well understood what factors cause the formation of a stone. Genetics, diet and dehydration contribute for the stone formation. Infectious bacteria form struvite stones [4].

The preferred management for kidney stones, when small enough, is observation of the patient to see if the stone will pass on its own. The likelihood of spontaneous stone expulsion depends on stone size: 80% of small stones smaller than 5 mm in diameter pass spontaneously, but under 30% of stones larger than 6 mm in diameter pass spontaneously [5]. If a stone does not pass spontaneously, a patient is treated with ureteroscopy, shock wave lithotripsy (SWL) or percutaneous nephrolithotomy (PCNL) based on size, composition and location of stones in a kidney. In ureteroscopy, a flexible ureteroscope with a camera is inserted through the urethra to reach a stone. Lasers are inserted through the ureteroscope, and stones are pulverized into fragments which can be passed spontaneously.

Introduced in the 1980s [6], SWL is the only completely noninvasive treatment for kidney stones. In SWL, an electrohydraulic, electromagnetic, or piezoelectric source outside the patient generates shock waves that are focused on the kidney stone to shatter it into small fragments [7]. As per a study conducted by Oberlin et al., ureteroscopy was preferred in 54.2% cases whereas shock wave lithotripsy was used in 41.3% cases during 2003 to 2012 [8]. PCNL is employed in rarer, more complex cases involving patients with many or very large stones and entails inserting a 1-cm-diameter tube into the kidney through the back. The American Urological Association and the

European Association of Urology provide guidelines on when each surgery is most appropriate. All procedures have associated injury to the kidney or ureter and risks of complications.

1.2 Shock wave lithotripsy (SWL)

1.2.1 Acoustic characteristics of shock wave lithotripsy

The shape of the SWL wave is shown in Fig. 1.1. It represents a pulse with a sharp rise in acoustic pressure resulting in a very high amplitude compressive phase followed by relatively slower drop in pressure resulting in tensile phase. In general, the peak positive pressure (P_+) varies from 30-100 MPa while peak negative pressure (P_-) ranges between -5 MPa and -15 MPa [9]. Various physical parameters (acoustic energy, energy flux density etc.) are calculated from the waveform and have been correlated with rate of breakage. One of the other important parameters to describe the pressure field generated by this wave is focal width. It is defined by a contour where the value of peak pressure drops to half (-6 dB points). The area defined by the contour is often referred as focus of the transducer. A transducer fragments stones effectively if it smaller than size of the focus. This is explained in section 1.2.2.

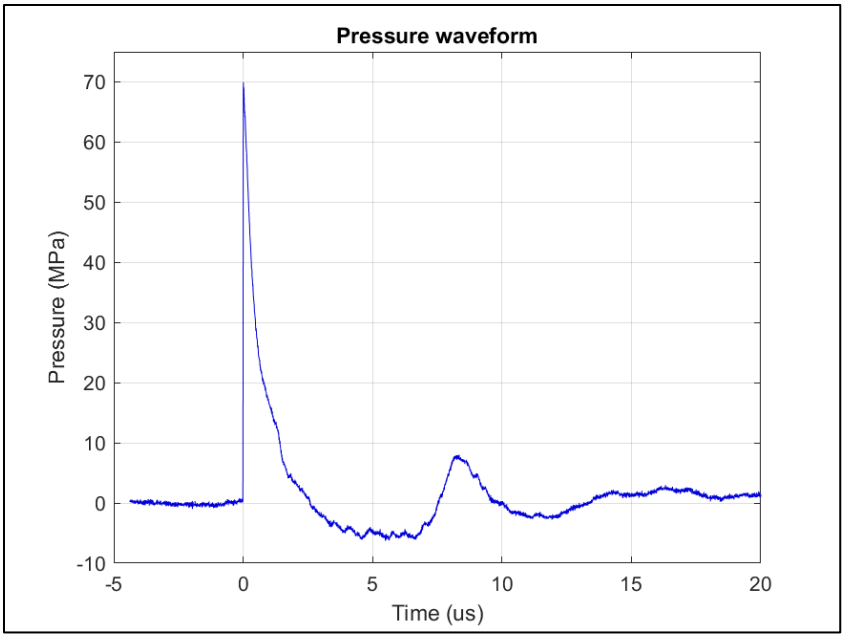

Figure 1.1 Waveform of a lithotripter - Dornier Compact S (Power level 5)

1.2.2 Mechanism of fragmentation

Many theories have been proposed describing process of fragmentation, however it is still not well understood enough to predict exact breakage pattern or its rate. Following table describes different theories explaining fragmentation of stones [10].

Table 1 Mechanisms of fragmentation of a stone in SWL

Hypothesis	Mechanism	Prerequisites	Type of action	Comments
Tear and shear forces [6]	Pressure gradients resulting from impedance changes at the stone front and distal surface with pressure inversion	Shock wave smaller in space extension than the stone	Hammer-like action resulting in a crater-like fragmentation at both ends of the stone	Only relevant for small focus zones

Spallation [11]	Reflected tensile wave at distal surface of the stone with maximum tension at the distal part of the stone	Shock wave smaller in space extension than the stone	Breaking the stone from the inside like freezing water in brittle material	Only relevant for small focus zones. No explanation for stone breakage at the front side
Quasi-static squeezing [12]	Pressure gradient between circumferential and longitudinal waves results in squeezing of the stone	Shock wave is broader than the stone Shock wave velocity is lower in the water than in the stone	Nutcracker-like action requiring large focal diameters	Only relevant for large focal zones
Cavitation [13]	Negative pressure waves induce a collapsing cavitation bubble at the stone surface	Low viscosity of surrounding medium	Microexplosive erosion at the proximal and distal ends of the stone	More important during stone comminution Useful for improving the efficiency of shock waves
Dynamic squeezing [14]	Shear waves initiated at the corner of the stone are reinforced by squeezing waves along the calculus	Parallel travelling of longitudinal waves. Shock wave velocity is lower in the water than in the stone	Nutcracker-like action in combination with spalling	Best theory to explain results of the numerical model

Based on the experiments carried out by Sapozhnikov et al.,[14] initial fragmentation is best described by dynamic squeezing. This theory accounts for all acoustic phenomena – inside and outside of the stone. After the initial fragmentation, the cavitation induced erosion is observed as

the cavitation is generated by the negative pressure phase in the microcracks and fluid surrounding the stone. Suppression of cavitation using highly viscous fluid or high pressure reduces efficacy of the procedure [15]. Based on these theories and more importantly on clinical performance, efforts have been put to improve efficacy of the procedure. Use of broader focus and low-pressure lithotripters has gained popularity as the research has shown that focal widths affect stone breakage in several ways [16].

1.2.3 Limitations of SWL

Although SWL became widespread after its introduction, young urologists are less likely to use it[8]. Newer lithotripters appear to have reduced success rates compared to first-generation lithotripters. New lithotripters replaced water baths with coupling cushions. Bohris showed that an 8% reduction in coupling required 43% more impulses for the same amount of fragmentation [17]. Another problem is localization of the stones. Targeting is difficult because of respiratory movements. Systems with respiratory belts and shock wave triggering did not penetrate the market due to long treatment times. Increasing pulse repetition frequency (PRF), the rate at which shocks are administered, may be thought as one the solutions to reduce the treatment time, however, PRF has negative correlation with the stone breakage. The cavitation during fragmentation limits choice of PRF. Bubbles formed during a pulse shield the next pulse if they are not given sufficient time to decay. Pishchalnikov et al. have shown that stone breakage was significantly better at 30 SW/min than at 120 SW/min [18]. Studies have shown that peak positive pressure is not affected by increasing PRF but peak negative pressure is [19]. Further, shock waves induce renal trauma primarily at vessels and tubular cells. Cavitaiton is considered the primary factor is tissue injury

but localized strains from just the shock wave may also contribute. Hence, there is a need for a non-invasive solution which eliminates these limitations of SWL.

1.3 Burst wave lithotripsy (BWL)

A new ultrasound-based technology has been developed by Maxwell et al. for breaking kidney stones [20]. It is inspired from high-intensity focused ultrasound (HIFU) and from studies of SWL showing effects of wide focus and low-pressure amplitude. In HIFU induced cloud cavitation research, a beam is strongly focused on surface of a stone to generate cavitation bubbles which erode the stone into fine dust [21], [22]. However, in BWL a low-pressure beam is broadly focused on a stone having similar or smaller width than the focus. This is hypothesized to generate strong shearing forces in the stone and disintegrate it into fragments. The bursts consist of multiple cycles of a sinusoidal wave instead of a single shock. (Figure 1.2)

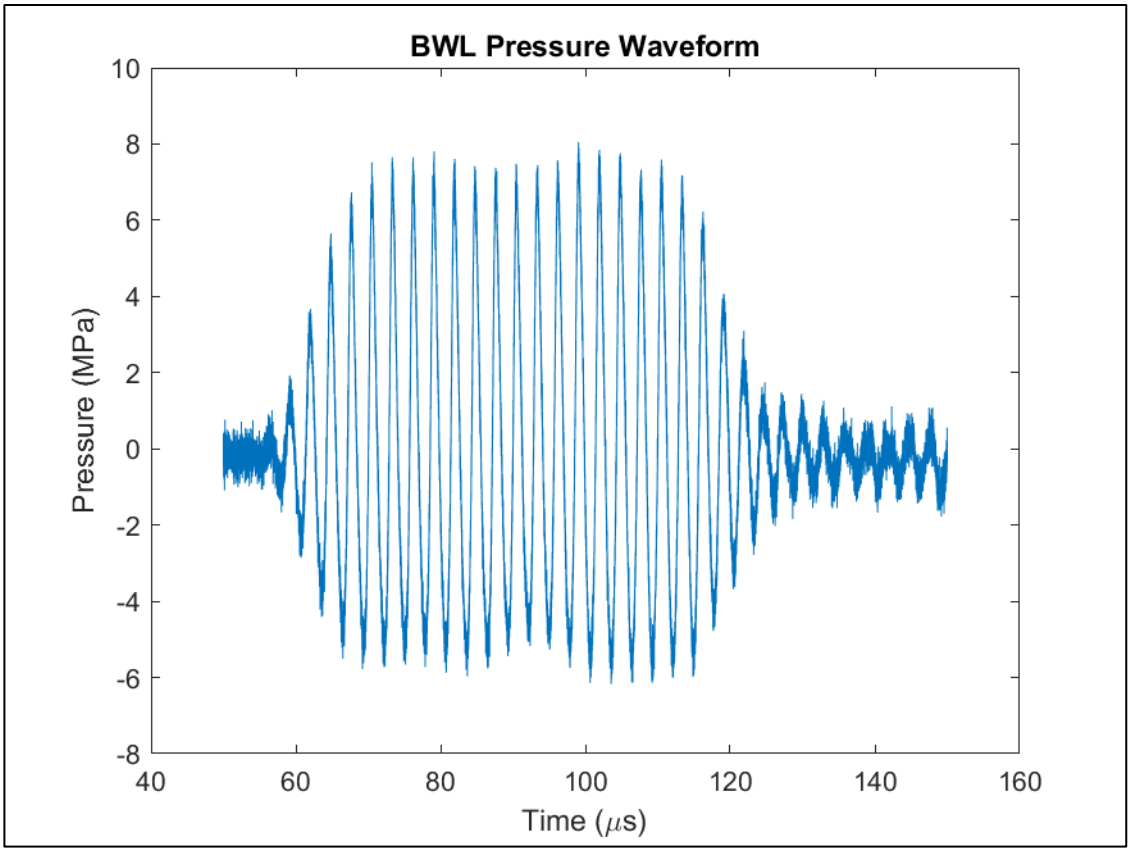

Figure 1.2 BWL waveform at 350 kHz

One of the notable features of BWL is that the size of the fragments can be controlled by changing frequency of the sinusoidal wave. The amplitude of bursts (~ 6.5 MPa) is low as compared to SWL and it prevents accumulation of cavitation bubbles even at PRFs higher than in SWL. This allows increased PRF up to ~100 Hz to maximize energy delivery to the stone. Avoiding accumulation of cavitation bubbles away from the stone surface also reduces risk of renal trauma. As the amplitude of the pressure is small as compared to SWL, the damage to tissues from shear and tear forces is expected to be less. Heating effects on tissue are not expected to cause damage as the operating frequency is lower than the HIFU applications used for thermal ablations and the time-averaged

power is low. Further, beams are broadly focused and hence have low spatial-peak temporal average intensity of approximately 15 W/cm^2 which is not sufficient for thermal ablation [20].

1.3.1 State of the art of BWL

When Maxwell et al. invented the technology in 2013, they fragmented artificial and natural stones of size 8.2 ± 3 mm at 170 kHz, 285 kHz and 800 kHz. The amplitude of pressure was 6.5 MPa or less with PRF of 200 Hz. Artificial stones were made from Begostone Plus plaster with similar acoustic properties to calcium oxalate monohydrate [24], [25]. Diameter of the stones was 6 mm and their length was 10 mm. It was found that the artificial stones could be fragmented at pressures as low as 2.8 MPa. 12 artificial stones were fragmented at 170 kHz and 6.5 MPa in 9.7 ± 2.8 minutes. When artificial stones were broken at 800 kHz, size of all the fragments was less than 1 mm. The size of fragments was less than 2 mm and 4 mm for stones treated at 285 kHz and 170 kHz respectively. Soft natural stones like uric acid and struvite stones were found to be broken in a few seconds in some cases. However, COM and cystine stones needed longer exposure for fragmentation. BWL is still under development and burst wave parameters need to be optimized for each type of stone. *In vivo* studies are being conducted in a porcine model to study injuries resulting from treatments. May et al. have shown injury is small even when outputs are increased specifically to form injury and also these injuries can be detected using ultrasound imaging. They studied how BWL affects kidneys in pigs and have evaluated renal injuries. The pigs were treated with transducers having frequencies 170 kHz and 335 kHz [23].

1.3.2 Challenges of BWL

As mentioned earlier BWL is still under development and various parameters like amplitude, frequency, PRF, number of cycles in a burst need to be optimized for breaking diverse type of stones effectively. Further, until now most of the experiments were conducted in vitro where the size of the transducer was chosen large enough to generate required focal pressure and focal width. For *in vivo* experiments in farm pigs, a common animal model for lithotripsy studies, available acoustic window is small (~80 mm) and focal distance cannot be varied over a broad range as the kidney stone is located 80 mm - 90 mm deep. Further, in Ch. 3 we will study how focal width is inversely proportional to frequency whereas the focal gain is directly proportional to frequency (focal gain is defined as the ratio of focal pressure to surface pressure of a transducer). The size of fragments of a stone is dependent on the center frequency. A higher frequency exposure will generate smaller fragments. Currently, frequencies between 300 kHz and 400 kHz are being studied as they produce fragments small enough to pass spontaneously and fragment a stone within a time window comparable to shock wave lithotripsy. These constraints limit our choice to vary frequency, focal distance and aperture of a transducer to obtain focus larger than 6 mm with required focal pressure. Hence, it becomes difficult to fragment a stone larger than 6 mm in a time window acceptable for a medical treatment.

1.4 Scope of the thesis

This research work is focused on broadening beam of a BWL transducer and forming focus large enough to break stones up to 12 mm with an 80 mm diameter transducer focused between 80 mm and 90 mm. To break stones effectively in a time window acceptable for a medical treatment, attempts are made to achieve focal pressure about 6.5 MPa for an operating frequency between

300 kHz and 400 kHz. In Ch.2, results of various experiments studying effects dust produced during fragmentation with shock wave lithotripsy on different kind of stones are presented. Different in vitro models to mimic in vivo conditions more accurately are explored. In Ch.3, procedures for designing a BWL transducer and its components are explained. Ch.4-6 focus on what modifications are introduced in the design of components of BWL transducer to achieve required focal pressure even when focus is broader than the existing BWL transducers. Ch.4 explores whether a porous PZT material can generate acoustic power required for achieving focal pressure for the broadened focus. Ch. 5 introduces a new method – holographic acoustic lenses for designing arbitrary shaped focus within given constraints. Ch. 6 details how this method can be used to broaden the focus. Finally, in Ch. 7, results of the experiments of fragmenting large stones (12 mm in length and 6 mm in diameter) with a transducer fabricated with the porous PZT material and the lens producing enlarged focus are presented.

References:

[1] C. D. Scales, A. C. Smith, J. M. Hanley, C. S. Saigal, C. S. Urologic Diseases in America Project, and U. D. in A. Project, "Prevalence of kidney stones in the United States.," *Eur. Urol.*, vol. 62, no. 1, pp. 160–5, Jul. 2012.

[2] E. M. Worcester and F. L. Coe, "Nephrolithiasis," *Prim. Care Clin. Off. Pract.*, vol. 35, no. 2, pp. 369–391, Jun. 2008.

[3] M. S. Litwin and C. S. Saigal, "Urologic Diseases in America," *Washington, DC US Gov. Print. Off. 2012; NIH Publ. No. 12-7865*, p. Tables: 11-2-11-42, 2012.

[4] J. C. Simon, A. D. Maxwell, and M. R. Bailey, "Some Work on the Diagnosis and Management of Kidney Stones with Ultrasound," *Acoust. Today*, vol. 13, no. 4, pp. 52–59, 2017.

[5] A. Ueno, T. Kawamura, A. Ogawa, and H. Takayasu, “Relation of spontaneous passage of ureteral calculi to size,” *Urology*, vol. 10, no. 6, pp. 544–546, Dec. 1977.

[6] C. Chaussy, W. Brendel, and E. Schmiedt, “EXTRACORPOREALLY INDUCED DESTRUCTION OF KIDNEY STONES BY SHOCK WAVES,” *Lancet*, vol. 316, no. 8207, pp. 1265–1268, Dec. 1980.

[7] M. R. Bailey, J. A. Mcateer, Y. A. Pishchalnikov, M. F. Hamilton, and T. Colonius, “PROGRESS IN LITHOTRIPSY RESEARCH,” *Acoust. Today*, vol. 2, no. 2, pp. 18–29, 2006.

[8] D. T. Oberlin, A. S. Flum, L. Bachrach, R. S. Matulewicz, and S. C. Flury, “Contemporary Surgical Trends in the Management of Upper Tract Calculi,” *J. Urol.*, vol. 193, no. 3, pp. 880–884, Mar. 2015.

[9] R. Cleveland and J. McAteer, *Simth’s Textbook on Endourology 1; The Physics of Shock Wave Lithotripsy*. Hamilton, ON: B. C. Decker Inc., 2007.

[10] J. J. Rassweiler *et al.*, “Shock Wave Technology and Application: An Update,” *Eur. Urol.*, vol. 59, no. 5, pp. 784–796, May 2011.

[11] P. ZHONG, X. XI, S. ZHU, F. H. COCKS, and G. M. PREMINGER, “Recent Developments in SWL Physics Research,” *J. Endourol.*, vol. 13, no. 9, pp. 611–617, Nov. 1999.

[12] W. Eisenmenger, “The mechanisms of stone fragmentation in ESWL.,” *Ultrasound Med. Biol.*, vol. 27, no. 5, pp. 683–93, May 2001.

[13] L. A. Crum, “Cavitation Microjets as a Contributory Mechanism for Renal Calculi Disintegration in Eswl,” *J. Urol.*, vol. 140, no. 6, pp. 1587–1590, Dec. 1988.

[14] O. A. Sapozhnikov, A. D. Maxwell, B. MacConaghy, and M. R. Bailey, “A mechanistic analysis of stone fracture in lithotripsy.,” *J. Acoust. Soc. Am.*, vol. 121, no. 2, pp. 1190–202, Feb. 2007.

[15] M. Delius, W. Brendel, and G. Heine, “A mechanism of gallstone destruction by extracorporeal shock waves.,” *Naturwissenschaften*, vol. 75, no. 4, pp. 200–1, Apr. 1988.

[16] W. Eisenmenger *et al.*, “The first clinical results of ‘wide-focus and low-pressure’ ESWL,” *Ultrasound Med. Biol.*, vol. 28, no. 6, pp. 769–774, Jun. 2002.

[17] C. Bohris, “Quality of coupling in ESWL significantly affects the disintegration capacity—how to achieve good coupling with ultra-sound gel,” *Ther. energy Appl. Urol. II Stand. Recent Dev.*, pp. 61–64, 2010.

[18] Y. A. Pishchalnikov, J. A. McAteer, J. C. Williams, I. V Pishchalnikova, R. J. Vonderhaar, and R. J. VonDerHaar, “Why stones break better at slow shockwave rates than at fast rates: in vitro study with a research electrohydraulic lithotripter.,” *J. Endourol.*, vol. 20, no. 8, pp. 537–41, Aug. 2006.

[19] Y. A. Pishchalnikov *et al.*, “Cavitation selectively reduces the negative-pressure phase of lithotripter shock pulses.,” *Acoust. Res. Lett. Online*, vol. 6, no. 4, pp. 280–286, Nov. 2005.

[20] A. D. Maxwell *et al.*, “Fragmentation of urinary calculi in vitro by burst wave lithotripsy.,” *J. Urol.*, vol. 193, no. 1, pp. 338–44, Jan. 2015.

[21] T. Ikeda *et al.*, “Cloud cavitation control for lithotripsy using high intensity focused ultrasound,” *Ultrasound Med. Biol.*, vol. 32, no. 9, pp. 1383–1397, Sep. 2006.

[22] A. P. Duryea, A. D. Maxwell, W. W. Roberts, Z. Xu, T. L. Hall, and C. A. Cain, “In vitro comminution of model renal calculi using histotripsy.,” *IEEE Trans. Ultrason. Ferroelectr. Freq. Control*, vol. 58, no. 5, pp. 971–80, May 2011.

[23] P. C. May *et al.*, “Detection and Evaluation of Renal Injury in Burst Wave Lithotripsy Using Ultrasound and Magnetic Resonance Imaging,” *https://home.liebertpub.com/end*, Aug. 2017.

[24] Y. Liu and P. Zhong, “BegoStone—a new stone phantom for shock wave lithotripsy research (L),” *J. Acoust. Soc. Am.*, vol. 112, no. 4, pp. 1265–1268, Oct. 2002.

[25] E. Esch, W. N. Simmons, G. Sankin, H. F. Cocks, G. M. Preminger, and P. Zhong, “A simple method for fabricating artificial kidney stones of different physical properties,” *Urol. Res.*, vol. 38, no. 4, pp. 315–319, Aug. 2010.

2 The Effect of Dust on Fragmentation of Kidney Stones by Shock Wave Lithotripsy in Tissue Phantoms

2.1 Introduction

In Ch. 1, it was noted that shock wave lithotripsy (SWL) sends focused ultrasound waves through the skin to fragment renal calculi. However, shock wave lithotripsy has variable success at rendering patients stone-free, in part because of inconsistent fragmentation. Part of the energy of the shock wave may not reach the stone because of inadequate coupling, poor targeting, or anatomic obstruction such as ribs. The shock wave may also generate a cavitation bubble cluster proximal to the stone, which scatters energy and reduces effective comminution.[1],[2] Cavitation shielding is exacerbated by a faster shock delivery rate, because bubbles from a shock wave do not have time to dissolve before the next shock wave and therefore the number of bubbles grows.[3],[4] Cavitation shielding is also affected by conditions of the shock wave, such as power setting or amplitude, wave shape, and wave frequency and fluid conditions such as volume, gas content, and level of filtration.[4], [5] There is limited ability to affect fluid conditions in treatment, but if they are not mimicked accurately in an *in vitro* stone breakage experiment, shielding that occurs *in vivo* will not be accurately simulated. As a result, water is often filtered and degassed for *in vitro* experiments to remove bubbles and submillimeter particles. Small particles themselves have little effect on shock waves, but they serve as niduses for bubble nuclei.[6] Comminution of a stone produces debris that create a similar result. In an effort to develop accurate models for Burst Wave

Lithotripsy (BWL) and also understand the comminution process within the kidney collecting system, the effect of debris on comminution and confinement of the fluid space surrounding the stone was studied.

In this study, the effect of dust on stone comminution was considered through multiple experiments. Two types of artificial stones, one that creates dust and one that does not, were compared. In addition, the stones were fragmented with SWL in different types of tissue phantoms which varied in degree of confinement of fluid and dust around the stone. The least confined phantom allowed unhindered dispersion of dust into water in the tank whereas the most confined phantom – anatomic kidney model did not allow the dust to leave a calyx holding the stone. Further, the anatomic kidney phantom was irrigated to displace the dust actively during the fragmentation and observed changes in rate of comminution.

2.2 Materials and methods

2.2.1 Setup

The experimental configuration is shown in Figure 2.1. A 190-liter water tank was filled with deionized water filtered through a sediment filter with a nominal 0.5 µm pore size. At a temperature of 18° C, the water was degassed to maintain a gas concentration corresponding to 50% of the saturation level of dissolved oxygen[5],[7] (Oxi 330i meter with a CellOx 325 probe, WTW, Weilheim, Germany). A shock wave emitter (Compact S, Dornier MedTech, Webling, Germany) was coupled to the water tank to deliver shocks along a horizontal beam axis. The shock wave lithotripter was operated at a power level of 5 (range 1-6) and a repetition rate of 70 shocks/minute. The focal pressure waveform of the lithotripter at this power level was measured

using a fiber optic hydrophone (Model FOPH 2000, RP Acoustics, Leutenbach, Germany) and is shown in Figure 2.2.

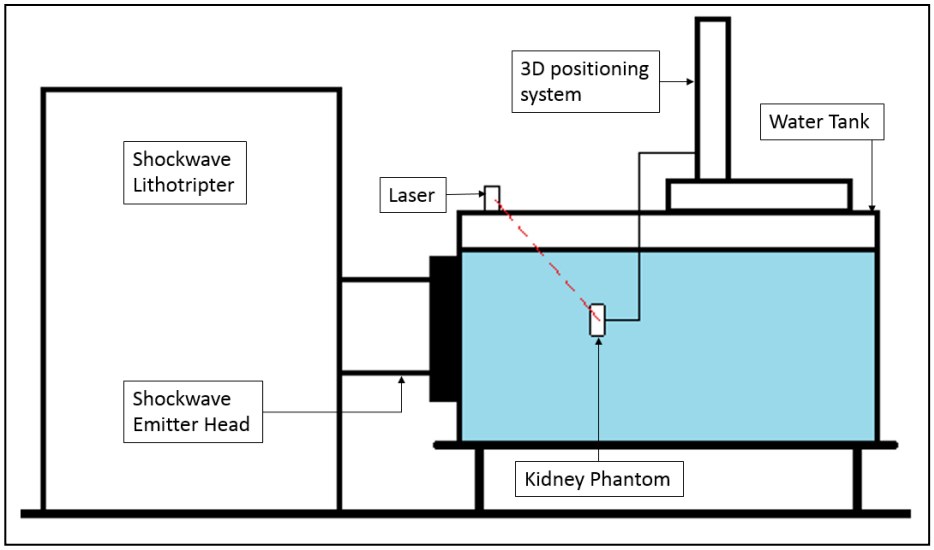

Figure 2.1 The figure shows set up of the experiment. A shockwave lithotripter was coupled with a water tank such that the shockwaves travelled horizontally. A kidney phantom holding the stone to be broken was positioned at the focus of the lithotripter with the help of 3D positioning system. The focus coincided with the intersection of two laser beams. The two lasers were placed on the side walls of the tank.

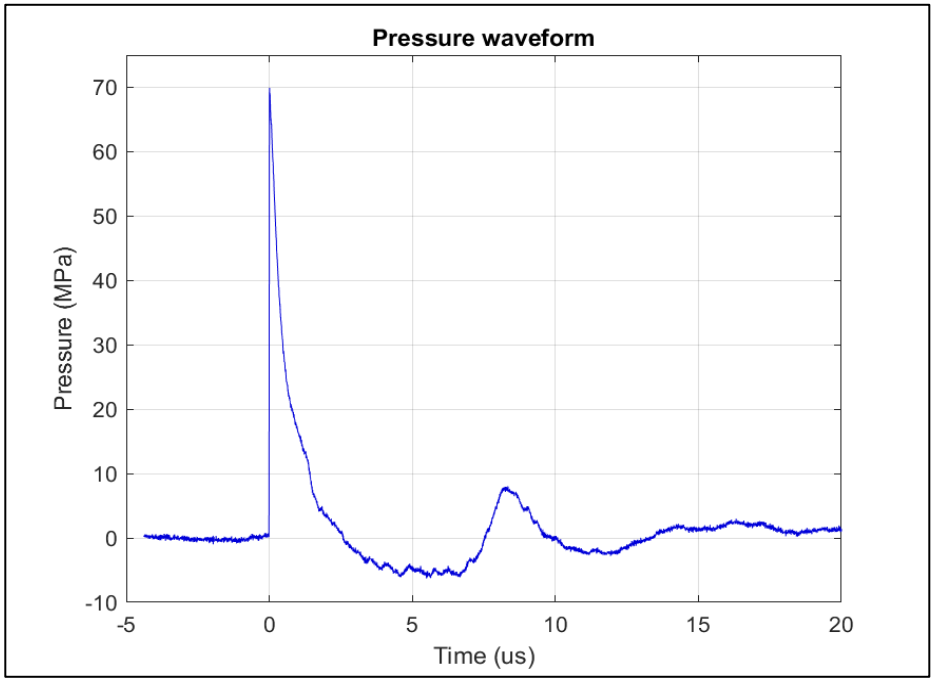

Figure 2.2 Pressure waveform of Dornier Compact S lithotripter. The lithotripter was operated at power level 5 and 70 shocks/min.

2.2.2 Phantoms

Different types of phantoms (Figure 2.3) were used for holding stones. Each phantom confined the fluid around the stone to a different degree. Phantom 1 was a semi-spherical shaped mesh basket made from nylon strands with 2 mm pores and a 35 mm diameter. Phantom 2 was a 60 mm diameter X 70 mm tall cylindrical "cup" made of polyvinyl chloride (PVC). The "cup" descriptor refers to the presence of a depression (15 mm diameter X 40 mm high) in the top flat surface. Shock waves entered from the side of the cup and traversed 22.5 mm of phantom before reaching the stone within the depression. Phantom 3 was the same PVC material and geometry, but with the top surface covered with Paraffin tape to further confine fluid around the stone and restrict the exchange of water between the depression and the bulk water in the tank. The speed of sound in the PVC is 1400 m/s and has attenuation comparable to human tissues.[8] Phantom 4 was an anatomical kidney model made from gelatin powder and water (Blue Phantom, Redmond, WA). This phantom has a sound speed of 1450 m/s and has little attenuation as compared to human tissue. The kidney phantom had a small slit at the ureteropelvic junction through which stones could be placed into the same mid-pole minor calyx for all experiments. The shock waves entered at a 90^0 angle to the anterior surface of kidney and the thickness of phantom traversed was 15 mm. Although the mesh basket from Phantom 1 is not associated with a volume per se, Phantoms 2–4 provide differing amounts of confinement for respective volumes of 7, 7, and 3 ml. The gels used are designed to mimic the acoustic properties of tissue. They cause minimum distortion in the transmitted shock wave which is confirmed for data from crystal stones in experiment 1. A combination of ultrasound imaging, a pointer, and lasers were used to assure alignment of the stone at the lithotripter focus.

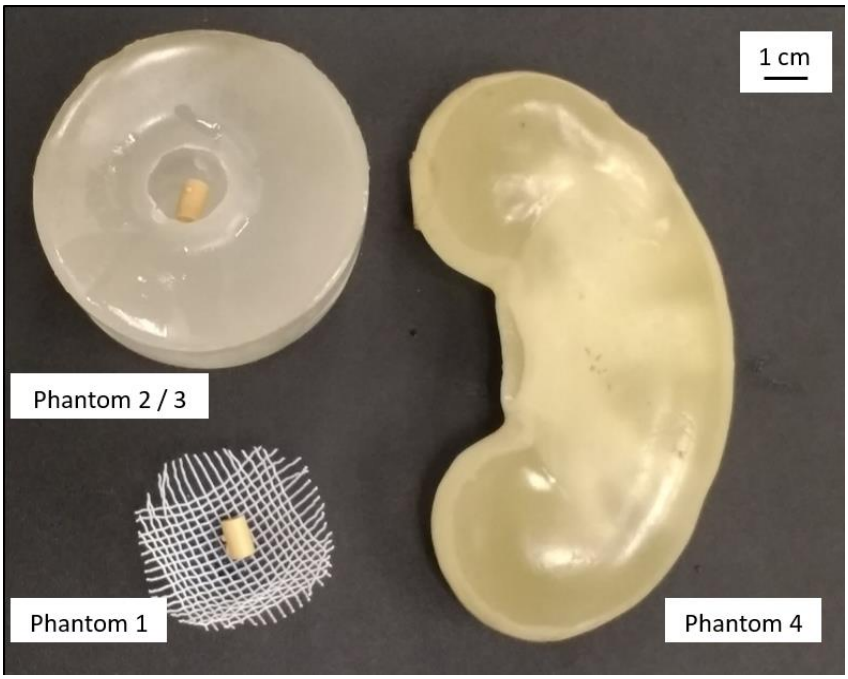

Figure 2.3 Tissue phantoms – Phantom 1: 2 mm mesh basket, Phantom 2: PVC cup, Phantom 3: PVC cup covered with Paraffin® tape and Phantom 4: anatomic kidney phantom.

We used plaster stones which emit dust during fragmentation and calcite crystal stones which do not. Artificial stones made from Begostone Plus plaster (Bego USA, Lincoln, RI), were formed into cylinders with two dimensions: 10 mm length X 6 mm diameter (avg. weight = 0.460 g) and 4 mm length X 6 mm diameter (avg. weight = 0.120 g). Prior to experiments, stones were hydrated for greater than 48 hours as recommended in the literature. Liu et al. have demonstrated the artificial stones made from Begostone Plus plaster have mechanical properties similar to natural stones and can be used as stone phantoms.[9] Calcite stones of Iceland spar (a crystalline form of calcium carbonate) weighed about 0.450 g and had sizes comparable to that of the large plaster stones. Blitz et al. have studied reproducible fragmentation of these stones that occurs in a linear relation with energy delivery and have demonstrated that it can be used as a stone model for lithotripsy[10].

2.3 Experiment

Experiment 1 compared the comminution rate for the four phantoms using the larger plaster stones and calcite stones. For each phantom, test stones were exposed for 15 minutes (1050 shocks) in steps of 5 minutes. Three stones of each type were broken in each phantom. Experiment 2 measured the comminution rate of plaster stones within Phantom 4 with different rates of water flow into and out of the phantom to remove dust and debris. The smaller plaster stones were exposed for 5 minutes (350 shocks) and 5 stones were broken in each of the following three flow rates: 0 cc/min (n=5), 7 cc/min. (n=5) and 86 cc/min (n=5). The 7 cc/min rate represents a rate near the upper bound for the maximum rate of induced urine production (9.5 cc/min) in the human kidney[11], while 86 cc/min rate is super-physiologic and is the maximum capable with the available infusion pump (Compact Infusion Pump - Model no. 975, Harvard Apparatus Co. Inc., MA). Water was injected through an 18-gauge needle into a mid-pole calyx of phantom 4. The irrigation system and the needle were present even when irrigant was not introduced.

After each shock wave exposure, stone fragments remaining in the phantom were collected and passed through a 2 mm sieve. The ratio of weight of fragments greater than 2 mm to the weight of the stone prior to exposure was calculated as a fragmentation metric. The mean and standard deviation for replicated measurements at the same time points are reported. The ratio $(W_i - W_f) / W_i$ reflects efficiency of the fragmentation as a fraction of the stone considered sufficiently fragmented for natural passage through the urinary tract, where W_i is the initial weight and W_f is the weight of remaining fragments greater than 2mm after the exposure. Except for phantom 1, all the pieces were returned to the phantom, where they were realigned for subsequent exposure. All the stones broke completely within 10 minutes in the phantom 1, hence we collected data in 5-minute steps for comparing effect of phantoms.

2.4 Results

In the first experiment, it was observed that dust clouds generated by erosion and fragmentation of the plaster stones drifted away from stones in phantom 1 (as shown in Figure 2.4) and phantom 2. When a fragment was smaller than the mesh size of phantom 1, it fell through the mesh and was collected in a plate at the bottom of the tank. Fragments did not leave the confined space in other phantoms. However, the incidence of each SW was observed to cause stones to jump around within each phantom, which necessitated occasional phantom repositioning to ensure that stones remained at the lithotripter focus.

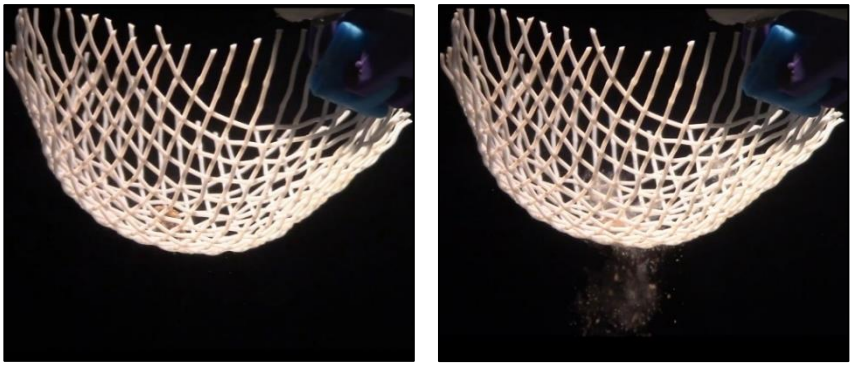

Figure 2.4 Dust clouds of a natural COM stone (about 5 mm in diameter) leaving phantom 1 during fragmentation.

Figure 2.5 shows the results of experiment 1 as comminution *versus* time for the 4 phantoms. For plaster stones, comminution effectiveness varied between phantoms: fragmentation after 5 minutes was 92 ± 2 % in phantom 1, 79 ± 6 % in phantom 2, 25 ± 3 % in phantom 3, and 19 ± 3 % in phantom 4. Thus, the phantoms where the dispersion of dust and convection of water were restricted showed lower comminution. Calcite stone fragmentation did not show the same trend, and after 5 minutes was 87 ± 3 % in phantom 1, 84 ± 1 % in phantom 2, 84 ± % in phantom 3, and 81 ± 3 % in phantom 4. There was significant difference between percentage of fragmentation of

phantom 1 and either phantom 3 or phantom 4 for plaster stones ($p<0.001$ in both cases) but not a significant difference for the analogous cases with the crystal stones ($p> 0.15$).

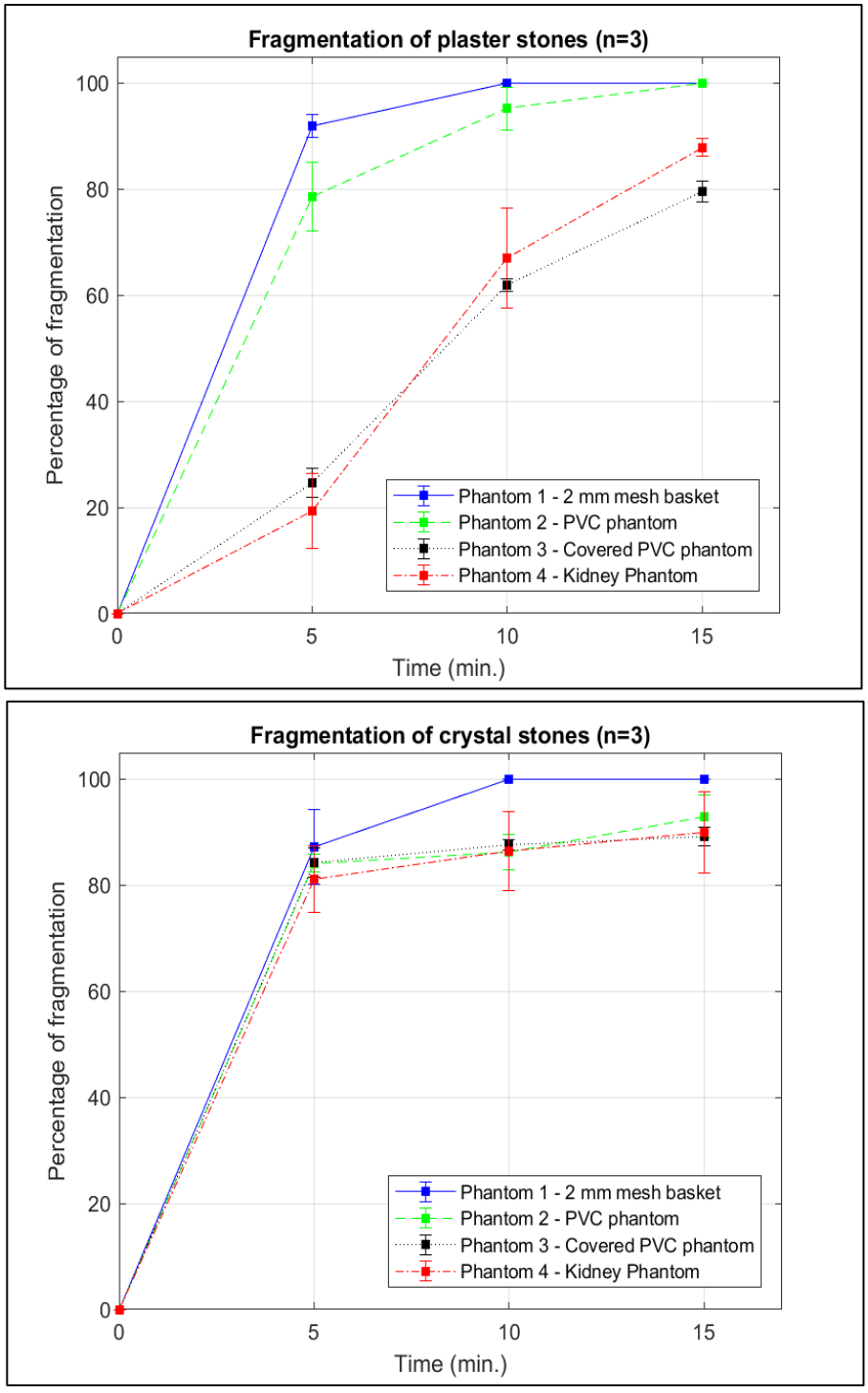

Figure 2.5 Effect of confinement on fragmentation of the stone - as the volume of confinement and dispersion of dust decreases, efficiency of the fragmentation of the plaster stones, which emit dust during fragmentation, decreases. Whereas, fragmentation of calcite crystal stones, which do not emit dust, is not affected by the phantom.

Figure 2.6 shows the results of experiment 2 as comminution *versus* irrigation rate. Fragmentation of plaster stones was 48 ± 17 % without irrigation, 51 ± 16 % with 7 ml/min, and 75 ± 10 % with 86 ml/min. The stones with the highest irrigation rate broke 27% better than stones without irrigation and the difference was statistically significant ($p < 0.01$). While irrigating at 86 cc/min, it was found that a few small fragments of the broken stone left the calyx with the flow of water and deposited in a calyx below it. However, these fragments were found to be smaller than 2 mm in size. It should be noted that larger stones were used in the experiment 1 to study confinement as compared to stones in experiment 2. Hence, the discrepancy in the percentages of stones breakage in the kidney phantom between experiments 1 and 2.

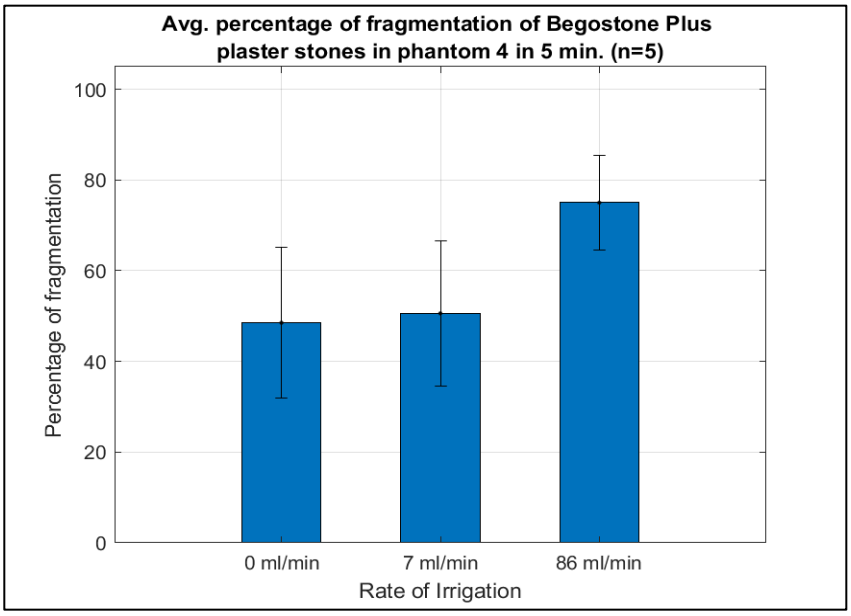

Figure 2.6 Effect of irrigation within phantom 4 – If water is infused in the kidney phantom continuously through a channel (and allowed to drain from other channel), stone dust is washed away resulting in increase in efficient of stone breakage. The percentage of breakage of plaster stones without irrigation in experiment 2 is higher than the percentage of breakage in experiment 1 with phantom 4 because the size of the stones in experiment 2 (4 mm diameter X 6 mm length) is smaller than the size of stones experiment 1 (6 mm diameter X 10 mm length).

2.5 Discussion

This study demonstrates that when dispersion of dust particles and convection of fluid are restricted, the efficiency of breakage of stones decreases for the plaster stones but not for the calcite crystal stones. The decrease in efficiency is likely due to stone dust which forms clouds around the stones and facilitates cavitation. Although other factors vary among phantoms, such as small differences in acoustic impedance, these differences had no apparent impact on the fragmentation of calcite stones. In contrast, the fragmentation of plaster stones changes when flow confinement is provided by either the PVC or kidney phantom. These phantoms impede dispersion of dust out of the area immediately surrounding the stone, and thus clouds surround the stone compactly. If there is sufficient removal or dispersion of dust around the stone, the density of cavitation decreases and efficiency of treatment increases. This is demonstrated by removal of the stone dust with active irrigation, efficiency of breakage of the stone increases. Furthermore, we performed this study at the lowest pulse repetition frequency (PRF) available on our lithotripter, and we anticipate the effect would be exacerbated at higher PRFs for which cavitation clouds can proliferate more easily.

As the efficiency of breakage increases to create more dust in the vicinity of the stone, it can be useful to move kidney stones from confined areas like small calyces to larger areas like the renal pelvis to treat them more effectively. With medication, humans can produce urine up to 9.5 ml/min in a kidney[11]. However, this rate of irrigation was not sufficient for significant improvement in efficiency in this study. Nonetheless, the result demonstrates that removal of the fluid containing the dust at a sufficient rate can improve lithotripsy. Certain acoustic exposures, such as those used in ultrasonic propulsion could induce acoustic fluid streaming in the urine[12], [13] and aid removal of such dust. Such exposures have been shown to enhance stone breakage during

lithotripsy *in vitro*[14]. Hence, potential future work may study how fluid streaming can be induced in the kidney such that there is considerable improvement in the efficiency of the treatment of the stone. Coupling these fluid streaming solutions can significantly improve efficiency of BWL system.

One of the limitations of the study is that it was conducted in phantoms and shock waves reached the phantom directly. In reality, the shocks pass through overlying tissues before reaching the kidney. Although all the phantoms had similar acoustic properties to most tissues, they were made from different materials which may produce a slightly different field on the stone. Additionally, the study was conducted with plaster stones which produce a large amount of dust. Natural kidney stones vary in composition and the relative quantity of dust produced during treatment also varies. Further, the gas concentration in a confined water volume was chosen to match cavitation threshold behaviors observed in pig kidneys *in vivo* for burst wave lithotripsy. Different threshold limits can be expected for SWL for cavitation. We note that the gas concentration used in these studies (50 % of saturation) is somewhat less than the 70 % present in urine[15], which should promote bubble dissolution to reduce cavitation effects[4]. Combined, this may result in variations in required treatment durations for phantoms and the human body. Future work is required to validate the hypothesis with natural kidney stones in a phantom and eliminate factors related to artificial stones.

2.6 Conclusion

Phantoms confining fluid motion around the stone were found to affect stone breakage in SWL. These observations imply that the dust around the stone and resulting cavitation shield the stone from shock waves and reduce efficacy of SWL. Fluid flow around the stone caused an increase in the efficiency of the treatment. The flow due to urine production in human kidney appears unlikely

to be sufficient to enhance breakage. Ultrasonic propulsion can be used for moving the debris away and should be integrated in BWL system for improving efficiency.

References:

[1] Y. A. Pishchalnikov, J. A. McAteer, J. C. Williams, I. V Pishchalnikova, R. J. Vonderhaar, and R. J. VonDerHaar, "Why stones break better at slow shockwave rates than at fast rates: in vitro study with a research electrohydraulic lithotripter.," *J. Endourol.*, vol. 20, no. 8, pp. 537–41, Aug. 2006.

[2] Y. A. Pishchalnikov, J. A. McAteer, M. R. Bailey, J. C. Williams, and O. A. Sapozhnikov, "Bubble proliferation in shock wave lithotripsy," *J. Acoust. Soc. Am.*, vol. 121, no. 5, pp. 3081–3081, May 2007.

[3] Y. A. Pishchalnikov and J. A. McAteer, "Cavitation-induced streaming in shock wave lithotripsy," *J. Acoust. Soc. Am.*, vol. 133, no. 5, pp. 3315–3315, May 2013.

[4] O. A. Sapozhnikov *et al.*, "Effect of overpressure and pulse repetition frequency on cavitation in shock wave lithotripsy," *J. Acoust. Soc. Am.*, vol. 112, no. 3, pp. 1183–1195, Sep. 2002.

[5] Y. A. Pishchalnikov, A. J. Zancanaro, J. C. Williams, and J. A. McAteer, "Gas content of the medium surrounding a stone has a significant effect on the efficiency of stone breakage in shock wave lithotripsy.," *J. Acoust. Soc. Am.*, vol. 127, no. 3, pp. 1761–1761, Mar. 2010.

[6] L. A. Crum and J. B. Fowlkes, "Acoustic cavitation generated by microsecond pulses of ultrasound," *Nature*, vol. 319, no. 6048, pp. 52–54, Jan. 1986.

[7] M. S. C Hunter, JS Ahn, W Kreider, AD Maxwell, BW Cunitz, Y Wang, B Dunmire, MR Bailey, JD Harper, “Evaluation of in vitro burst wave lithotripsy exposure conditions. Scientific Program of 35th World Congress of Endourology Program Book and Abstracts,” *J. Endourol.*, vol. 31, no. S2, p. (S2) paper BRPRS4-20, Sep. 2017.

[8] G. M. Spirou, A. A. Oraevsky, I. A. Vitkin, and W. M. Whelan, “Optical and acoustic properties at 1064 nm of polyvinyl chloride-plastisol for use as a tissue phantom in biomedical optoacoustics,” *Phys. Med. Biol.*, vol. 50, no. 14, pp. N141–N153, Jul. 2005.

[9] Y. Liu and P. Zhong, “BegoStone—a new stone phantom for shock wave lithotripsy research (L),” *J. Acoust. Soc. Am.*, vol. 112, no. 4, pp. 1265–1268, Oct. 2002.

[10] B. F. BLITZ, E. S. LYON, and G. S. GERBER, “Applicability of Iceland Spar as a Stone Model Standard for Lithotripsy Devices,” *J. Endourol.*, vol. 9, no. 6, pp. 449–452, Dec. 1995.

[11] S. M. Upsdell, S. M. Leeson, P. J. Brooman, and P. H. O’Reilly, “Diuretic-induced urinary flow rates at varying clearances and their relevance to the performance and interpretation of diuresis renography.,” *Br. J. Urol.*, vol. 61, no. 1, pp. 14–8, Jan. 1988.

[12] M. D. Sorensen *et al.*, “Focused ultrasonic propulsion of kidney stones: review and update of preclinical technology.,” *J. Endourol.*, vol. 27, no. 10, pp. 1183–6, Oct. 2013.

[13] H. C. Starritt, F. A. Duck, and V. F. Humphrey, “An experimental investigation of streaming in pulsed diagnostic ultrasound beams.,” *Ultrasound Med. Biol.*, vol. 15, no. 4, pp. 363–73, Jan. 1989.

[14] T. A. Zwaschka *et al.*, “Combined Burst Wave Lithotripsy and Ultrasonic Propulsion for Improved Urinary Stone Fragmentation,” *J. Endourol.*, p. end.2017.0675, Mar. 2018.

[15] E. Y. Hwang, J. B. Fowlkes, and P. L. Carson, “Variables controlling contrast generation in a urinary bladder model,” *J. Acoust. Soc. Am.*, vol. 103, no. 6, p. 3706, May 1998.

3 Designing a BWL Transducer

3.1 Introduction

Traditionally, focused therapeutic transducers have been constructed from spherically curved segments of piezoelectric materials with frequencies ranging from 200 kHz to 5 MHz. Transducers required for research or clinical applications are manufactured by specialty companies and cost $5000-$20,000 with 1.5 to 6 months required for fabrication. Hence, custom fabrications of these transducers especially transducers with a large aperture and high focal gain have significant costs, causing difficulty to iterate designs for new applications. Hence, Kim et al. developed a rapid prototyping method for fabrication of focused ultrasound.[1] This method reduces development time and cost of fabrication substantially. To fabricate transducers with this method we need a housing, piezoelectric elements made from lead-zirconate titanate (PZT), a backing material, a matching layer, an acoustic lens. The transducer is then connected through a matching network to a signal generator and amplifier to power the transducer with appropriate pulsing scheme. This chapter details what specific materials are used for fabricating a BWL transducer. This is followed by how acoustic lenses, PZT elements, matching layer and matching network are modeled. Finally, steps for building a BWL transducer are provided. This background is helpful for understanding what modifications in the existing transducer can be introduced to generate a pressure profile with enlarged focus.

3.2 Materials

An exploded view of a BWL transducer is shown in Figure 3.1. The housing and lenses are fabricated using 3D printing technology (preferably with a stereolithography apparatus which has

resolution in range of 10-100 μm). They are fabricated with material suitable for acoustic transmission *i.e.* it has low attenuation and high sound speed to make thin lenses thin and has acoustic impedance suitable for higher transmission into load medium. It is found that the materials Accura 60® (3D Systems, Rock Hill, SC) and Veroclear® (Stratasys, Eden Prairie, MN) are suitable for this application. Sound speed and acoustic impedance of Veoclear are 2560 m/s and 3 MRayls respectively. PZT4 and PZ36 (Meggitt, Kvistgaard, Denmark) are used for generating pressure waves with amplitude more than 1 MPa at their surface. They can handle voltage up to 2500 V without irreversible damages when used with matching layer and a lens. A matching layer is useful to generate high bandwidth, increase electrical impedance of elements, improve transmission of energy and decrease internal stress in the element for a given surface pressure. The matching layer is made from epoxy-ceramic or epoxy-metal composites. A specific epoxy resin is chosen for its low viscosity (Pro Set INF-114 with its hardener Pro Set INF- 112; Gougeon Brothers Inc., Bay city, MI) and the second material is aluminum oxide (Al_2O_3) or tungsten (W). The acoustic impedance of the matching layer can be controlled by varying ratio of epoxy and the other material. The PZT elements are backed with a low-density but rigid polyurethane foam so that nearly all of the acoustic energy is transmitted into load medium and not into backing material.

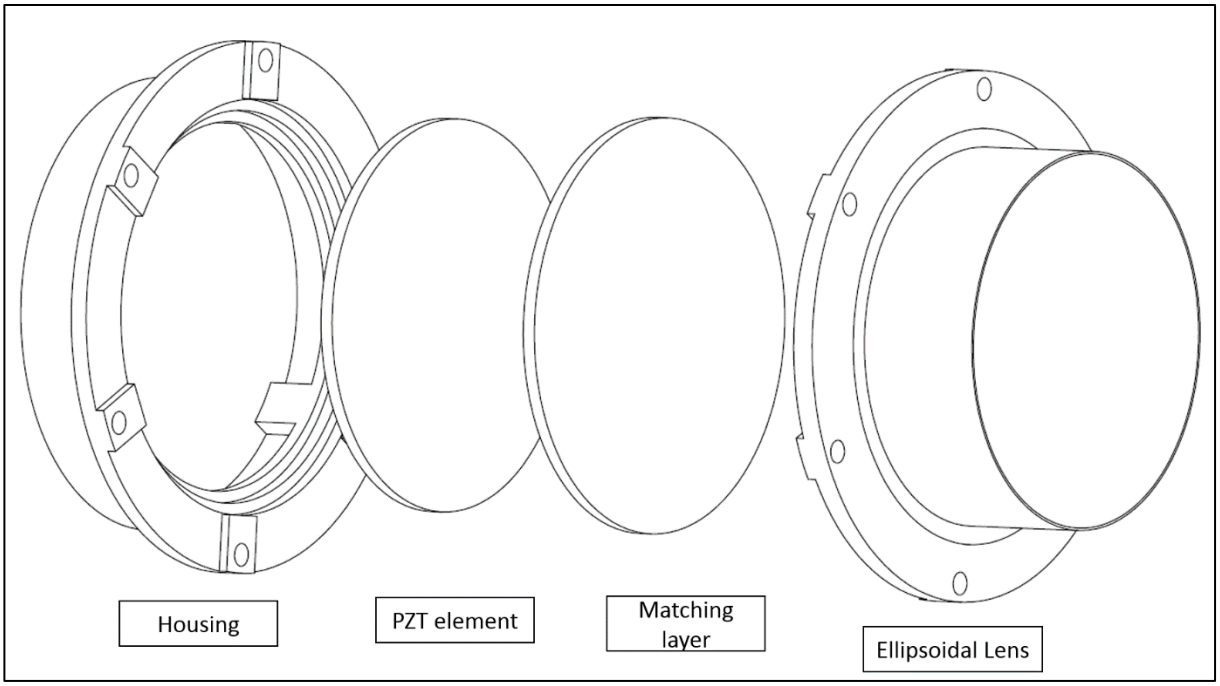

Figure 3.1 This is an exploded view of a BWL transducer. The housing of the transducer has supporting structures for PZT element on which a matching layer is spread uniformly. An ellipsoidal lens is clamped on top of the matching layer. The empty space in housing behind PZT material is filled with a backing material.

3.3 Modeling a transducer

a) Acoustic lens and its pressure field

First, frequency (*f*), focal distance (*d*) and diameter of the transducer (*2a*) are chosen based on the application of BWL transducer. Then, lenses are used for introducing phase difference at different points on the plane of the transducer. The interference patterns resulting from these wavefronts produce the required pressure field. The focal width of a perfectly focused spherical transducer is given by the equation:

$$Focal\ Width = \frac{\pi d}{ak} \qquad (1)$$

Where k is spatial frequency or wave number ($k = 2\pi f/c$, where c is speed of sound in the medium). Focal gain of a transducer for the same lens is given by the equation:

$$Focal\ Gain\ (G) = \frac{ka^2}{2d} \tag{2}$$

If we have a thin lens with radius of curvature r_c, the focal distance is given by

$$Focal\ Distance\ (d) = \frac{r_c}{1 - n_r} \tag{3}$$

where, n_r is ratio of speed of sound in surrounding medium to that of lens material. To eliminate spherical aberrations, elliptical lenses are designed with it eccentricity (ε) equal to n_r. The major axis and minor axes of the ellipse should equal to $d(1 + n_r)$ and $d\sqrt{(1 - n_r)(1 + n_r)}$ respectively.

Change in phase introduced by spherical or ellipsoidal lens is continuous and smooth. A Fresnel lens provides a structured way to introduce quantized phase changes at the surface of the transducer. With Fresnel lens, phase change is quantized by dividing 360° in to N steps. The height of each step (h) is given by

$$h = \frac{1}{Nf(1/c_{medium} - 1/c_{lens})} \tag{4}$$

where f is frequency, c_{medium} and c_{lens} are sound speed in surrounding medium and the lens material. [2] The radius (r_k) of kth phase step is given by[3]

$$r_k = \left[\left(d + k\frac{\lambda}{N}\right)^2 - d^2\right]^{0.5} \tag{5}$$

where k and λ are wave number and wavelength in the lens material. Efficiency of the Fresnel lens increases as number of steps is increased. Efficiency (η) is given by

$$\eta = \left[\frac{\sin(n/N)}{n/N}\right]^2 \quad (6)$$

where $2^n = N$. [2]

A numerical model of the Rayleigh integral can be used for calculating pressure in the field,

$$p(x,y,z) = \left[\frac{-jkp_0}{2\pi}\int_s \frac{e^{jkR}}{R}dS\right] \quad (7)$$

where p_0 is pressure at the surface of the PZT or surface of lens if there is a lens, *S* is surface of the PZT and *R* is distance of a point in pressure field from element *ds*. Focal gain can be calculated for an arbitrary shaped transducer using this formula. It should be noted that the integral does not account for non-linear effects.

Fundamental principles of holography can be applied to simulate pressure field for an arbitrary shaped transducer. This method is discussed in detail in Ch. 5.

b) KLM model of PZT elements

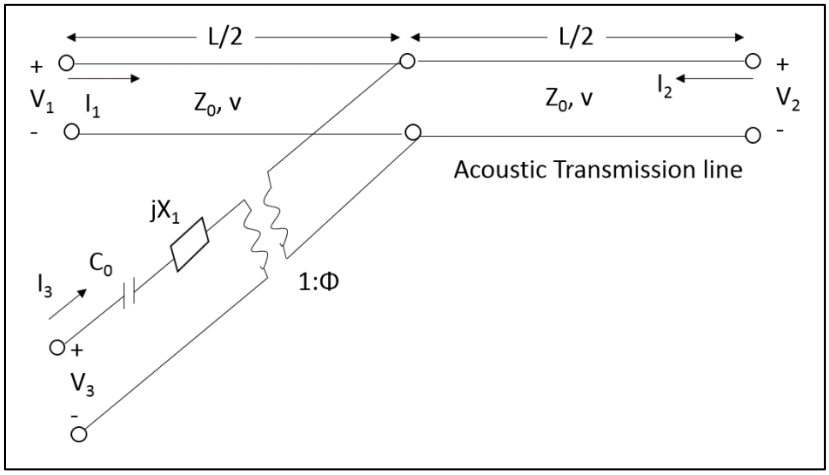

Figure 3.2 KLM Model of PZT elements

PZT elements are modeled using a model developed by Krimholtz, Leedom and Matthaei (KLM model).[3] Based on this model, formula for calculating electrical input impedance of an element and pressure radiated by a surface of PZT for an applied voltage are obtained. Electrical Input impedance (Z_{in_KLM}) near resonance frequency is given by

$$Z_{in\_KLM} \cong \frac{1}{j\omega C_0} + \frac{jh^2\pi}{\omega^2 Z_0}\left(1 - \frac{\omega}{\omega_0}\right) + \frac{4h^2}{\omega^2(Z_1 + Z_2)} \qquad (8)$$

where ω is angular frequency, C_0 is capacitance of the PZT element, h is piezoelectric pressure constant, Z_0 is acoustic impedance of the PZT, ω_0 fundamental resonant frequency, Z_1 is acoustic impedance of backing material and Z_2 is acoustic impedance of load material.[4] Pressure radiated at the surface facing load medium is given by

$$p_2(w) = \frac{Z_2 V_3(\omega)(\Gamma_1 e^{-jkd/2} - e^{jkd/2})}{\phi Z_{in\_KLM}(e^{jkd} - \Gamma_1\Gamma_2 e^{-jkd})}(1 + \Gamma_2) \qquad (9)$$

And pressure radiated in backing material is given by

$$p_1(w) = \frac{Z_1 V_3(\omega)(e^{-jkd/2} - \Gamma_2 e^{jkd/2})}{\phi Z_{in\_KLM}(e^{jkd} - \Gamma_1\Gamma_2 e^{-jkd})}(1 + \Gamma_1) \qquad (10)$$

where V_3 is voltage across the PZT, d is thickness of PZT, k is wavenumber in PZT, $\phi = \omega Z_0/2h$, $\Gamma_1 = \frac{(Z_0 - Z_1)}{(Z_0 - Z_1)}$ and $\Gamma_2 = \frac{(Z_0 - Z_2)}{(Z_0 - Z_2)}$.[4]

If we have a PZT element, it impedance can be calculated using impedance vs. frequency response analyzer. The element has only real impedance at it resonating frequency. The resonance frequency can be estimated from sound speed in the element and thickness of the element. Thickness of the element is a quarter of the wavelength at the resonance frequency. Hence, resonance frequency is given by

$$f_{resonance} = \frac{C_{element}}{2 \times t_{element}} \quad (11)$$

where, $C_{element}$ and $t_{element}$ are sound speed and thickness of the element respectively. It should be noted that the impedance of an element at a given frequency varies with acoustic impedance of the backing material and loading medium. Hence, it is specific to the design used for testing. If same set of backing material and loading medium are used in designing a new transducer, we can estimate impedance of the elements used in the transducer with the equation,

$$A \times Z_{in} = const. \quad (12)$$

where A is area of the PZT element and Z_{in} is electrical input impedance. Further, if efficiency of the transducer (Acoustic Intensity/ Electrical Intensity) is known for the test element, the acoustic power output a new transducer can be calculated for a given input voltage. First, average electrical power in a pulse is calculated by

$$P_{electric\_pulse\_Avg} = \frac{|V_{mn}|^2}{Z_{in\_mn}} \quad (13)$$

where V_{mn} is rms (root mean square) voltage applied across the matching network (discussed below in 3.3 c) and Z_{in_mn} is electrical impedance of the PZT with matching network at the resonance frequency. Second, electrical intensity is calculated by dividing $P_{electric\_pulse\_avg}$ by area of the element. Third, acoustic intensity is calculated by multiplying efficiency of the transducer and electrical intensity. Finally, acoustic power output of a new transducer is calculated by multiplying acoustic intensity and area of PZT elements in the transducer.

c) Matching layer

As a wave travels across a boundary of two media, a part of the wave is transmitted and a part of it is reflected. The transmission and reflection coefficients for normally incident sound wave are given by

$$T = \left(\frac{2Z_2}{Z_1 + Z_2}\right) \quad (14)$$

$$R = \left(\frac{Z_2 - Z_1}{Z_1 + Z_2}\right) \quad (15)$$

where Z_1 and Z_2 are acoustic impedances of the media (the wave travels from medium 1 to medium 2). Matching layer is required when there is low power transmission due to mismatch of the acoustic impedances of the two media. Desired acoustic impedance of the matching layer is calculated from different formulae which assume different boundary conditions. In our case we used formula given by Souquet which assumes finite length of the PZT material (backed by air) and calculates impedance for matching layer of a quarter wavelength in it.[5]

$$Z_{matching} = \sqrt[3]{2Z_1Z_2^2} \quad (16)$$

Thickness of matching layer should be $\lambda_{matching}/4 \pm \lambda_{matching}/30$ where $\lambda_{matching}$ is wavelength of sound in matching layer. $\lambda_{matching}/4$ is the optimal thickness of effective transmission with 1 dB loss at resonance frequency. Change in thickness of matching layer result in significant losses. Souquet et al. have shown that if the thickness of the matching layer is within above mentioned tolerances, the losses are less than 3 dB. [5]

d) Matching Network

A matching network for each element of a transducer is required for altering power output from an amplifier to the transducer. The matching network is connected between amplifier and the elements. Once we know real and imaginary parts of the impedance of an element at a desired frequency, we can use L-bridge step-down matching network to get desired impedance. The desired impedance depends on the specifications of the power source and amplifier.

3.4 Steps for designing and fabricating a BWL transducer

1. Choose frequency, focal distance and diameter of the transducer based on the specific application, focal width and focal gain.
2. Model pressure field using Rayleigh integral. Iterate the parameters to achieve desired focal width and focal gain. Otherwise, an acoustic lens can be designed using holographic techniques described in Ch.5.
3. Choose PZT material for generating sufficient surface pressure so that required focal pressure is achieved for required focal width. Use KLM model to predict acoustic output.
4. Calculate acoustic impedance of the matching layer to determine its composition, speed of sound, density and thickness.
5. Design a housing accommodating the focusing lens, PZT element and matching layer.
6. Fabricate the transducer, measure impedance of each element and design a matching network.
7. Characterize the transducer to confirm the focal gain, focal width and pressure field.

3.5 Conclusion

Fabricating a BWL transducer with rapid prototyping technique reduces cost and duration of the development. This allows us to iterate changes in the design of the various components of the transducer. These components include housing, PZT elements, matching layer, acoustic lenses and a matching network. They can be designed using existing theoretical models to meet specific design requirements. Finally, a step by step procedure of rapid prototyping technique can be followed to fabricate the transducer and validate the performance.

References:

[1] Y. Kim, A. D. Maxwell, T. L. Hall, Z. Xu, K.-W. Lin, and C. A. Cain, "Rapid prototyping fabrication of focused ultrasound transducers," *IEEE Trans. Ultrason. Ferroelectr. Freq. Control*, vol. 61, no. 9, pp. 1559–1574, Sep. 2014.

[2] B. Hadimioglu, E. Rawson, R. M. Lujan Lim, J. C. Zesch, B. T. Khuri-Yakub, and C. F. Ouate, "HIGH-EFFICIENCY FRESNEL ACOUSTIC LENSES," *Ultrason. Symp. IEEE*, pp. 579–582, 1993.

[3] R. Krimholtz, D. A. Leedom, and G. L. Matthaei, "New equivalent circuits for elementary piezoelectric transducers," *Electron. Lett.*, vol. 6, no. 13, p. 398, 1970.

[4] Unknown_author, "APPENDIX B: THE KLM MODEL."

[5] J. Souquet, P. Defranould, and J. Desbois, "Design of Low-Loss Wide-Band Ultrasonic Transducers for Noninvasive Medical Application," *IEEE Trans. Sonics Ultrason.*, vol. 26, no. 2, pp. 75–80, Mar. 1979.

4 Determination of Maximum Pressure Output by Piezoceramic Elements

4.1 Introduction

In Ch. 1, we noted that a focal beamwidth of 12 mm and focal pressure of 6.5 MPa are needed for breaking larger kidney stones effectively. However, increasing the beamwidth while maintaining pressure amplitude requires greater power emitted from the transducer. The acoustic power emitted from a transducer is calculated from surface pressure of the transducer. Following equation relates acoustic power and acoustic intensity of a transducer to the surface pressure of the transducer.

$$\begin{aligned} Acoustic\ Intensity \\ &= \frac{Acoustic\ Power}{radiating\ area\ of\ transducer} \\ &= \frac{p_{surface}^2}{2\rho c} \end{aligned} \qquad (17)$$

where ρ is density of water and c is speed of sound in water. Based on this equation, acoustic power can be increased only by increasing surface pressure of the transducer given that we have fixed radiating area. If we assume that the enlarged focus is a circle with diameter 12 mm and has focal pressure 6.5 MPa evenly distributed in it, required acoustic power is 1593 W. If this much power is supposed to be generated from a transducer having circular radiating area with diameter 80 mm, minimum required surface pressure is about 1 MPa. However, these estimations assume that all the radiated power is transmitted to the enlarged focus. In practice, a fraction of energy is lost in

area outside the focus. Further, the radiating surface area is not continuous as PZT elements are divided in sectors for obtaining appropriate electric impedance. Hence, a fraction of radiating surface is lost in supporting structures of the PZT elements. Also, one needs to consider attenuation losses in the matching layer and lens material. All of these factors result into requirement of higher surface pressure than the estimated surface pressure. Hence, piezoelectric material that could produce surface pressure more than 1 MPa needed to be explored. Here, PZ36 (Meggitt, Kvistgaard, Denmark) was tested as a potential piezoelectric material to produce required pressure. The elements were tested with and without matching layer and a lens. The tests were designed to determine the acoustic power output for a voltage applied across a PZT element and what level of voltage can be achieved prior to irreversible damage to the test element. Along with that, electric current and electric power were noted. Finally, surface pressure was calculated from the measured acoustic power.

4.2 Materials and methods

PZ36 is a porous piezoceramic developed for high intensity focused ultrasound applications. Sound speed, density and acoustic impedance of PZ36 are 2874 m/s, 6269 kg/m^3 and 18 MRayls respectively. PZ36 elements were 3.62 mm thick and their resonance frequency was 400 kHz. They were cut into 25 mm by 25 mm squares using a dicing saw and held in housing shown in Figure 4.1 (a). The elements were connected to an L-bridge step down network and impedance of the combinations were matched to 20 Ω. The measured impedance of the elements varied between 17 Ω to 22 Ω. The phase values of the impedances were less than 10° in all the cases.

The schematic of setup of the experiment is shown in Figure 4.1 (b). The elements were powered with an amplifier developed in the lab connected to a high voltage power supply (GENH600, TDK-

Lambda, Tokyo, Japan). The voltage from the power supply ranged between 50 V and 330 V and was increased in steps of 10 V. The elements were operated at frequency of 335 kHz in burst mode for a chosen pulse repetition frequency (PRF). The number of cycles in a burst were chosen between 20 and 50. PRF was varied between 20 and 500. The elements were operated thrice for a minute for an input voltage from the power supply. The elements radiated pressure waves into a cup filled half way with sound absorbing material made from silicone and the remainder filled with degassed and deionized water. The cup rested on a laboratory balance (ENTRIS6231-1s, Sartoris, Goettingen, Germany) and weight measurements were recorded with a MATLAB script. These measurements were processed further to calculate average acoustic power during the operation. Peak-to-peak voltage across the elements was measured with a P4100 high voltage probe (100 MΩ impedance and attenuation 100:1) connected to an oscilloscope (InfiniiVision MSOX3034T, Keysight, Santa Rosa, CA). Hence, all the voltages reported in the chapter are peak-to-peak voltages. Current in the element was measured with a current transformer (Model 110, Pearson Electronics, Palo Alto, CA) connected to the same oscilloscope. The multiplication operation on the oscilloscope calculated power supplied to the element. The power was averaged over 10 cycles of the waveform in steady state. The measured acoustic power was averaged over time; hence pulse average of the acoustic power was calculated using duty cycle of the wave. The surface pressure was calculated using equation (17).

(a)

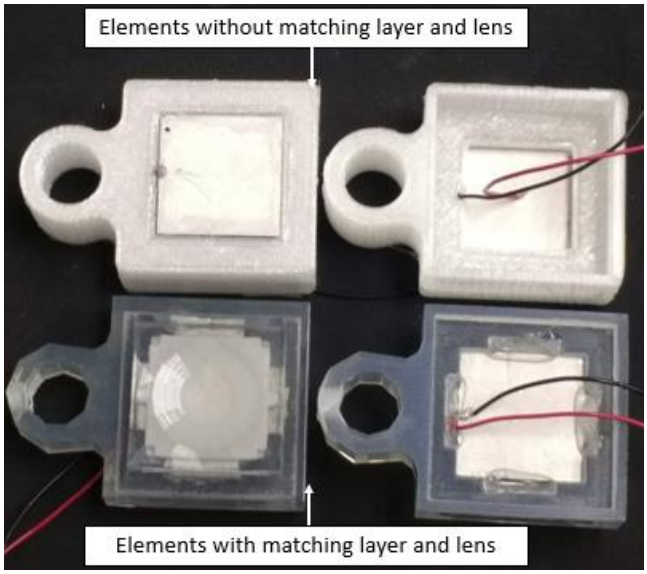

(b)

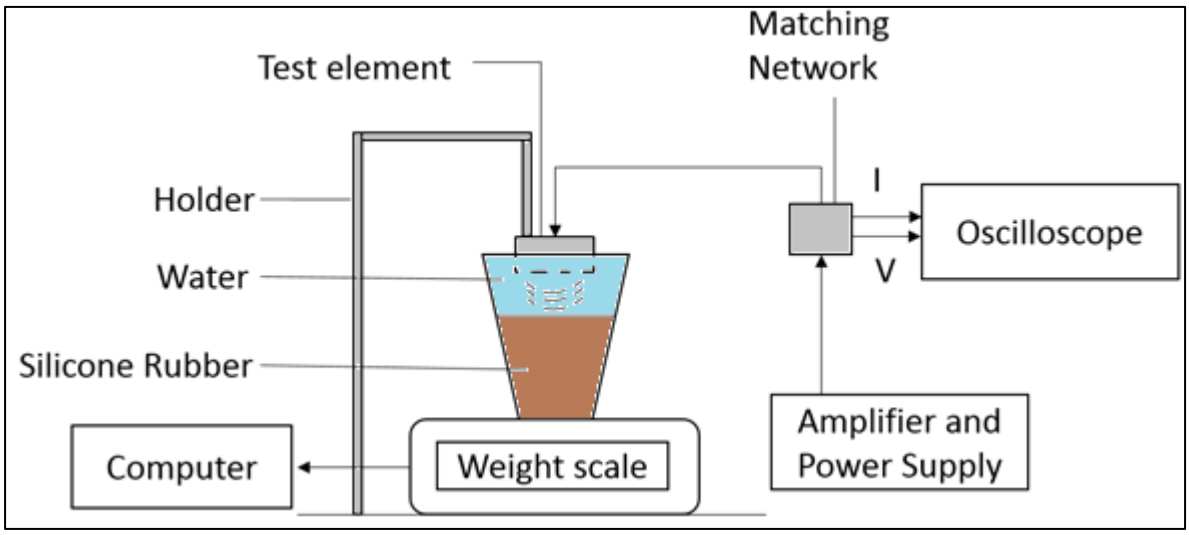

Figure 4.1 The PZT elements were held in a housing as shown in (a). Top row shows PZT elements without matching layer and lens material (front and back). The bottom row shows PZT elements with matching layer and lens material (front and back). Schematic of the experimental set up is shown in (b). The radiating surface of a test element was submerged in water in the upper half of the cup. The lower half was the cup was filled with silicone rubber which absorbed acoustic radiation. The radiation force was measured by the balance. The signal from the amplifier and power supply was transmitted to the element through impedance matching network. Voltage and current after the matching network were measured with appropriate probes connected to the oscilloscope.

4.3 Results

Figure 4.2 shows how surface pressure, electric intensity and acoustic intensity varies with voltage across one of the elements. As more voltage was applied to the elements, it produced more acoustic power, but it starts to decrease after a point. The elements had irreversible damage when voltage across the elements was more than 1000 V except one which failed at 1300 V. Modes of the failure included detachment of connecting wire from the PZT and mechanical cracks on the surface of the PZT. Average maximum surface pressure amplitude was 0.47 ± 0.08 MPa when the elements were operated around 800 V at 350 kHz with a burst having 50 cycles and pulse repetition frequency of 500.

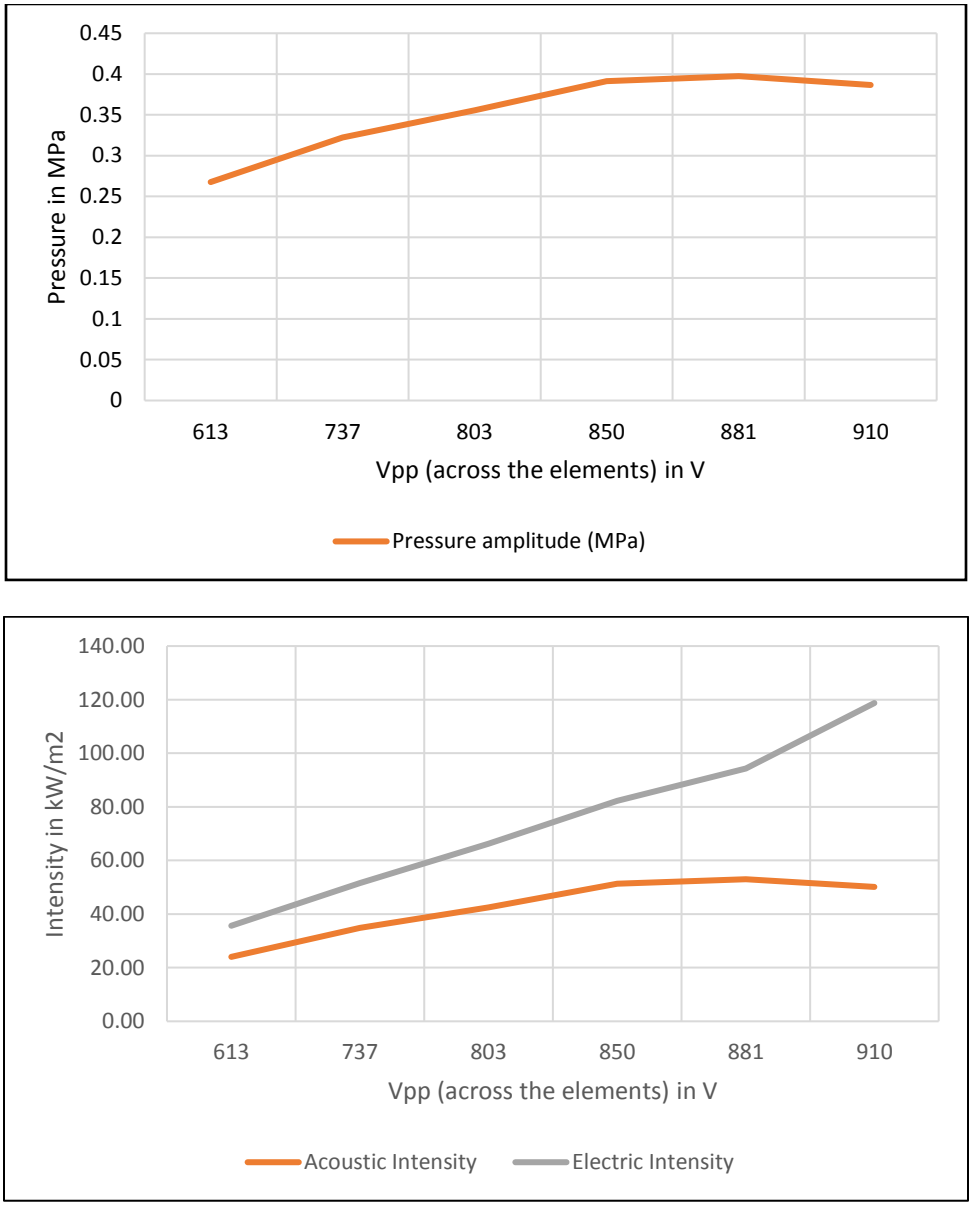

Figure 4.2 When voltage across an element without matching layer was increased, the surface pressure (Top) and acoustic intensity (bottom) increased up to a limit. The acoustic output drops when the applied voltage exceeds 900 V. The elements have irreversible damage above 1000 V. Maximum surface pressure produced by this element is 0.39 MPa at 881 V (peak to peak).

Figure 4.3 shows how surface pressure, electric intensity and acoustic intensity increase with applied voltage across the elements with matching layer and lens. These elements did not have any

irreversible damage even when the voltage across the elements exceeded 2800 V. Heating was observed at higher voltages when the PRF was more than 20. Hence PRF was changed from 500 to 125, 50 and 20 with increase in voltage across the element. It was adjusted to avoid heating in the elements but still get enough power to measure on weight scale. It was found that average maximum surface pressure was 1.47 ± 0.02 MPa when the elements were operated at 350 kHz with pulse repetition frequency of 20 of a burst having 20 cycles. Voltage across the elements was between 2750 and 2900 when they produced their highest-pressure amplitude. Further increase voltage resulted in decrease in acoustic intensity and surface pressure. The elements did not have irreversible damage up to 3200 V.

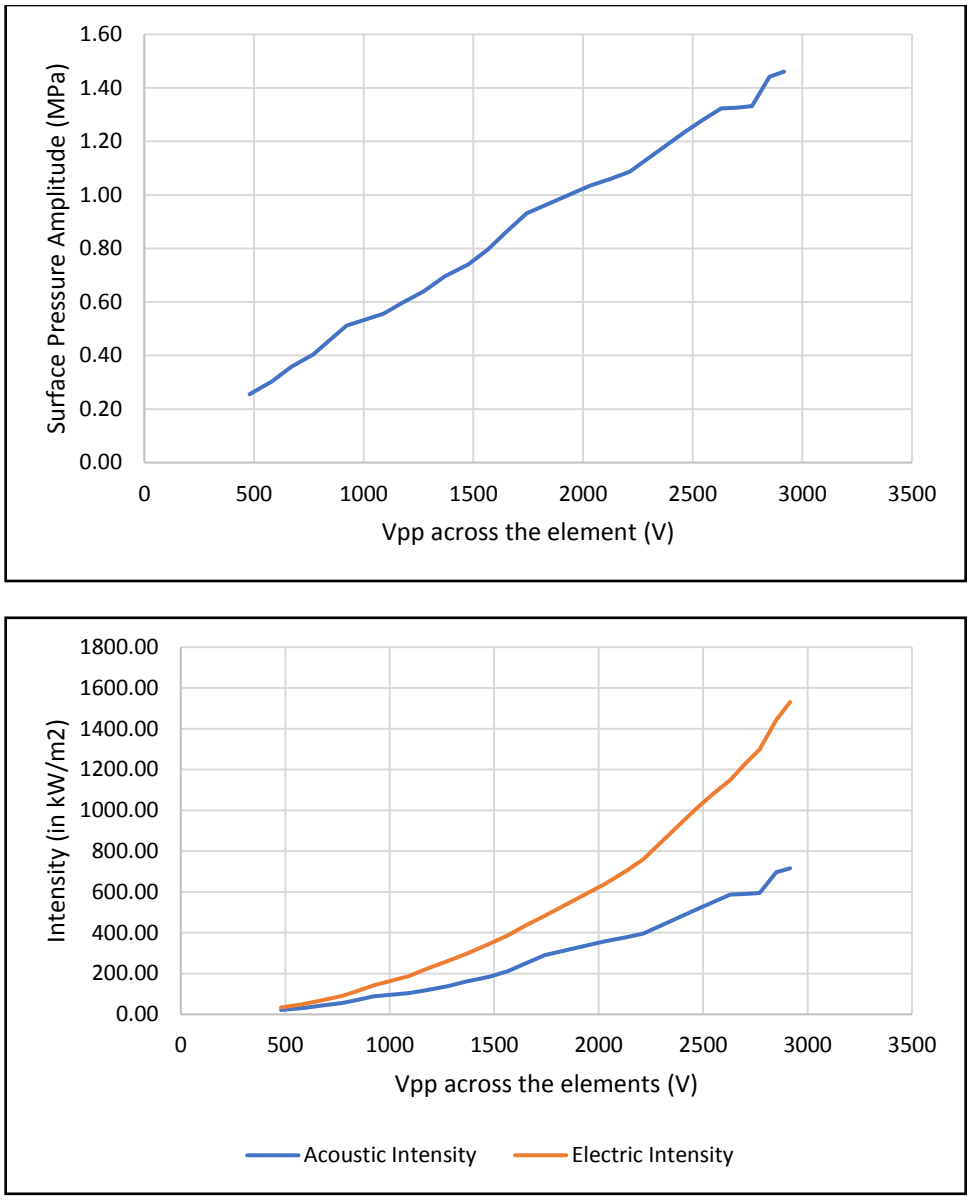

Figure 4.3 When applied voltage across the elements with matching layer and lens is increased, there is linear increase in surface pressure of the element (Top). Maximum observed surface pressure for this element was 1.46 MPa at 2917 V. PRF of the signal was adjusted to avoid heating in the elements at higher voltages. Efficiency of the element (Bottom) decreases from 64% at 480 V to 47% at 2917 V. Elements with matching layer and lens did not have irreversible damage even when voltage across the elements was 3200 V.

4.4 Discussion

When elements were tested without matching layer and lens, they showed a linear increase in surface pressure with increase in voltage across the elements. However, when peak-to-peak voltage exceeded 900 V, the surface pressure reached an asymptote. The maximum surface pressure in this situation was about 0.5 MPa, which is not sufficient for broadly focused transducer. The elements failed when vibrations of the elements resulted in detachment of the wires. The cracks were initiated near spots where wires were soldered to PZT. This suggests that soldering material concentrated over a very small area may cause development of excess stress in the element.

When the PZT was tested with matching layer and lens, the stresses were minimized. There was no irreversible damage to the elements up to 3200 V. The surface pressure increased linearly with voltage across the PZT. Maximum surface pressure produced by these elements was about 1.4 MPa which meets the requirement mentioned in the beginning of the chapter. The observed heating in the elements with increase in voltage is attributed to dissipative losses in the vibration of the elements. This results in decreased efficiency (defined as ratio of acoustic output power to electric input power). As the PRF of the signal is lowered, the total dissipative losses are reduced, and heating is avoided. However, this reduces the average acoustic output over a time period larger than the burst of the wave. This average acoustic power is measured by the balance. Hence, the PRF and pulse duration applied to the elements needed to be balanced to measure significant changes in the measurements of the scale. It should be noted that lowering PRF reduces total dissipative losses over a time period larger than burst but not for a single burst. Hence, efficiency dropped even when heating was avoided but higher voltage was put across the element. Efficiency dropped from 64% at 480 V to 47% at 2917 V.

One of the challenges of the study was to maintain accurate measurement of the voltage across the elements. As the range of the voltages varied from 480 to 2917 V, different dynamic ranges on the oscilloscope were required. Hence, it was observed that different elements produce same highest surface pressure between 2750 and 2919 V. Further, drifts in the measurements of the scale were observed frequently throughout the measurements. The MATLAB script measured weight before and after the operation of the element to estimate the drift and correct it. The scale measurements were adjusted as per the estimated drift.

4.5 Conclusion

PZ36 material was tested with and without a matching layer and lens to determine if it can generate a surface pressure greater than 1.2 MPa. The PZT can generate up to 0.47 MPa without a matching layer and failed when more than 1000 V was put across the element. When the PZT was tested with a matching layer and lens, it generated surface pressure up to 1.47 MPa. The highest surface pressure was achieved when voltage applied across the elements varied between 2750 and 2900 V. However, the PRF of the signal needed to be adjusted to avoid heating in the element and generate the highest surface pressure with the matching layer and lens. These elements did not have any irreversible damage even when 3200 V was applied.

5 Design, Fabrication and Validation of Holographic Lenses with Iterative Angular Spectrum Approach

5.1 Iterative angular spectrum approach

The iterative angular spectrum approach (IASA) is a method for manipulating wavefronts in a 3D volume. Currently, the acoustic wavefronts are manipulated by using phased array transducers (PATs) in which each pixel is addressed by an independent transducer. Marzo et al. have built holographic acoustic elements for manipulation of levitated objects in air.[1] The PATs are dynamic and can be programmed in real time. However, cost of PATs increases unfavorably for generating wavefronts with higher resolution as it needs a higher number of elements to achieve high accuracy in the wavefronts. Melde et al. have used a hologram technique but implemented it with phase encoded lens which was fabricated by inexpensive rapid prototyping technique.[2] This technique achieves reconstruction degrees of freedom two orders of the magnitude higher than commercial phased array sources. It scales well to higher information content in the hologram, larger aperture size and higher power.[2] These characteristics are suitable for high intensity ultrasound applications. Hence, this technique was explored for generating larger focus. This chapter discusses the algorithm, its implementation and validation. A perfectly focusing lens and a complex pressure field producing lens were designed with the algorithm. They were fabricated and coupled with a plane transducer. Their pressure fields were scanned in the focal plane to confirm the output simulated by the algorithm. The pressure field of perfectly focusing holographic lens was compared with pressure field of an equivalent ellipsoidal lens. Once it was confirmed that the algorithm was implemented successfully, the algorithm was used to design holographic lenses

which produce larger focus. The techniques for producing larger focus are discussed in the next chapter.

5.2 Algorithm for designing holographic lens

As per the IASA discussed by Melde et al., a desired pressure profile in a plane (desired image) is given as input to the iterative angular spectrum algorithm. The distance of the image from the plane of the transducer can be chosen per requirement. The algorithm treats pixel values of the image as desired peak pressures at those points in the plane. Then, it propagates the acoustic field from the plane of the transducer to image plane and back to the transducer plane to find out phase distribution on the surface of the transducer. The phase distribution is realized by fabricating an acoustic lens. The thickness of the lens at each pixel is calculated based on the required phase, speed of sound in water and speed of sound in the lens material. Mellin et al. have formulated the steps of this algorithm for optical holograms and Melde et al. adapted these for acoustic holograms.[2], [3] They have also extended this technique to produce different images at different distances from the plane of the transducer. The steps of the algorithm are as follows:

1. Use Fourier transform to represent pressure field in angular spectrum.

   Pressure in spatial three-dimensional space is described by

$$p(x,y,z) = \hat{p}(x,y,z)e^{j\Delta\Phi(x,y,z)} \qquad (18)$$

where $\hat{p}(x,y,z)\ and\ \Delta\Phi(x,y,z)$ are the amplitude and phase functions. This pressure field is represented in angular spectrum with following Fourier transform equation

$$p(k_x,k_y,\mathrm{z}) = \iint_{-\infty}^{+\infty} p(x,y,z)e^{-j(k_x x + k_y y)}\,dxdy \qquad (19)$$

2. Propagate the field from the hologram to each image plane using following equation for forward propagation of wave.

$$p(k_x, k_y, \mathrm{z}) \;=\; \mathrm{P}(k_x, k_y, 0) e^{jz\sqrt{k^2 - k_x^2 - k_y^2}} \qquad (20)$$

3. Use following inverse Fourier transform equation to represent the wave in spatial coordinates and evaluate the quality of the projected image for each image plane.

$$p(\mathrm{x}, \mathrm{y}, \mathrm{z}) \;=\; \frac{1}{4\pi^2} \iint_{-\infty}^{+\infty} P(k_x k_y, z)\, dk_x dk_y \qquad (21)$$

4. Reset the amplitude for each image plane to match the target value. The forward-propagated phase is retained.
5. Separately propagate the field for each image plane back to the hologram.
6. Sum all back-propagated complex fields in the hologram plane.
7. Compute the thickness of the hologram pixels and the transmission coefficient $\alpha_T\,(x, y)$ using equations given below.

$$\alpha_T\,(x, y) = \frac{4 Z_t Z_h^2 Z_m}{z_h^2 (Z_t \,+\, Z_m)^2\, cos(k_h T(x, y))^2 \,+\, (Z_h^2 \,+\, Z_t Z_m)^2\, sin(k_h T(x, y))^2} \qquad (22)$$

where $Z_i \;=\; \rho_i c_i$ is the acoustic impedance of a medium. Subscripts *t*, *h* and *m* stand for transducer, hologram and the medium in which desired image lies. To calculate thickness of the hologram, we begin with thickness T_0 and thickness $\Delta T(x, y)$ is subtracted at each point.

8. Set the complex amplitude at the hologram plane to $\hat{p}\,(x, y, 0) = \sqrt{\alpha_T}\widehat{p_0}(x, y)$.
9. Repeat from step 1 until desired image quality is achieved.
10. Finally, calculate thickness of the lens with following equations,

$$\Delta\Phi(x, y) = (k_m - k_h)\Delta T(x, y) \tag{23}$$

where $T(x, y) = T_0 - \Delta T(x, y)$.

5.3 Materials and methods

5.3.1 Fabrication of a plane transducer

A plane transducer was fabricated with PZT4 material but without matching layer (Figure 5.1 (a)). It was operated between 300 kHz and 400 kHz. The transducer was coupled with different acoustic lenses to generate desired pressure profiles. The lenses were fabricated with rapid prototyping machine (Object30 Pro, Stratasys, Eden Prairie, MN) and VeroClear® as prototyping material. The pressure profiles were scanned in an 80-liter water tank (Figure 5.1 (b)) with a hydrophone (HNR-0500, Onda, Sunnyvale, CA). The transducer was fixed in the tank, and a hydrophone scanned pressure profile in a transverse plane or along the z-axis. Position of hydrophone was controlled with a 3D positioning system (Xslide, Velmex, Bloomfield, NY). The waveform of the received signal was observed on an oscilloscope. The data collected at each point in a plane were recorded and post-processed to measure strength of a signal at a frequency. Step size between recorded points on oscilloscope was less than the wavelength. Finally, focal widths of pressure profiles were measured with the help of graphical representation of pressure fields corresponding to a dominant frequency component.

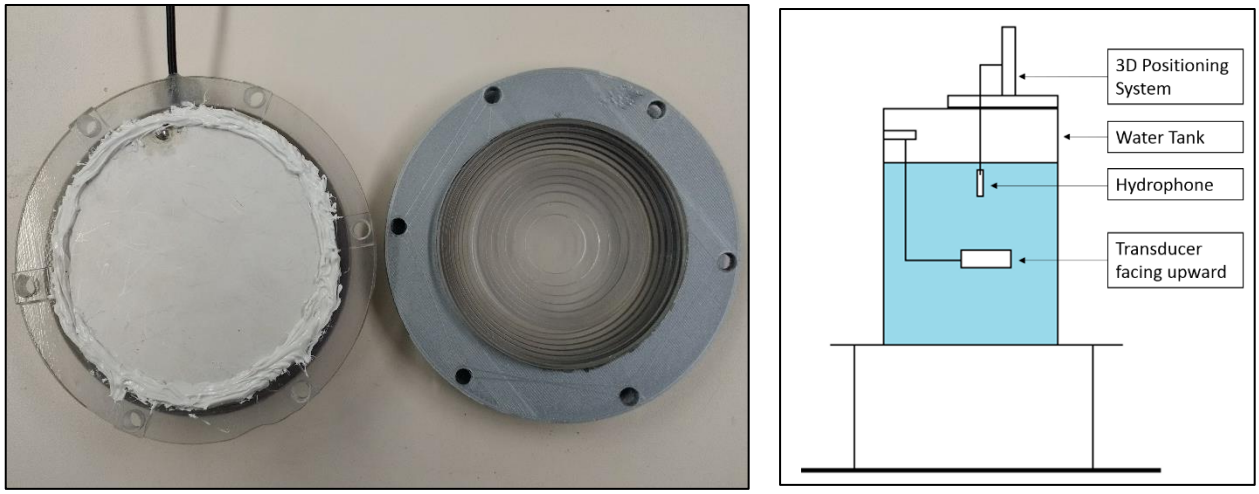

Figure 5.1: (a)A plane transducer was fabricated and coupled with different lenses for generating desired pressure profiles. The image shows a transducer with a lens (b) Schematic of set up used for scanning pressure profiles

5.3.2 Implementation of the algorithm

The algorithm was implemented using MATLAB®. A mesh grid four times the size of the diameter of the transducer was created with spatial resolution of 0.2 mm. This allowed all the spectral components originating from image or the hologram to propagate without aliasing. The binary values (0 or 1) of pressure were chosen in the transducer plane to represent the amplitude distribution on the transducer surface as shown in Figure 5.2(a). Values of various parameters used in various iterations in this chapter and next chapter were as follows:

Table 2 Parameters used in developing acoustic holograms with IASA

Frequency	300, 335, 350 and 400 kHz
Sound speed in water	1500 m/s
Sound speed in hologram	2560 m/s
Sound Speed in PZ36	2874 m/s
Sound speed in PZT4	4390 m/s
Density of water	1000 kg/m^3
Density of hologram	1200 kg/m^3

Density of PZ36	6269 kg/m^3
Density of PZT4	7550 kg/m^3
Outer diameter of therapeutic transducer	80 mm and 85 mm
Inner diameter of therapeutic transducer	26 mm, 36 mm and 40 mm
Focal Distance	78 mm to 105 mm

The desired image was represented with a matrix having same size as that of transducer plane. The image was converted into grayscale and rescaled to fit size of the matrix with padding of zeros as per requirement. To achieve stark contrast, the image can be binarized further. Finally, angular spectrum grid (k_x, k_y, k_z) was created, and transducer plane was forward propagated to image plane with angular spectrum wave representation.

The forward propagated pressure field in the image plane was calculated with inverse Fourier transform and compared with desired pressure field. If the error was not within acceptable limits, desired pressure amplitude was imposed but phase was conserved. The imposed pressure field was back-propagated to transducer plane and the amplitude of the transducer was imposed. The back-propagated phase values were used to calculate thickness of the hologram at each point in the mesh grid. Based on the thickness attenuation coefficient and resulting amplitude in the transducer plane was calculated. This procedure was repeated until the error between desired pressure field and forward propagated pressure field in image plane was within acceptable limits or until the iterations converged to a pressure field distribution (which may or may not be the desired pressure field) in the image plane. The number of iterations were restricted to 200. All the figures representing pressure field in transducer plane, phase profile of the hologram, thickness of the hologram, pressure field in image plane, pressure field 15 mm before and after the image plane were plotted. Finally, based on the thickness of hologram matrix, a .STL file of a lens was prepared using a MATLAB® script by Bill McDonald.[4]

5.3.3 Designing a lens for assembly

To design the lens for final assembly, the thickness matrix needs to be modified before converting it into a .STL file. Otherwise, the script generates square shaped hollow surface as one would observe the thickness matrix with *surf* command in MATLAB. The circular profile of the lens can be generated by assigning *NaN* to elements outside the diameter the transducer in the thickness matrix. Small thickness values produce weak parts in the lens. Hence, supporting base material of 3 to 5 mm to needs to be added to all the points. Further, the diameter of base material was set 90 mm, slightly larger than the transducer aperture to facitilitate attachment to the transducer face. A ring of 1 mm width and zero thickness was added after 90 mm diameter. This ring helps for setting boundary limits in Meshmixer® software used for converting a hollow body in to a solid body.

5.4 Simulations and validation

5.4.1 Validation with perfectly focused lens

To validate implementation of the algorithm, a focusing lens (d = 90 mm, f = 335 kHz) was designed, fabricated and tested against a perfectly focused ellipsoidal lens. The desired pressure field in the focal plane was a circular shaped image with 6 mm diameter. The results are shown in Figure 5.2. The shape of the simulated pressure field and measured pressure field is almost the same. The focal width predicted by algorithm is 6.8 mm and measured focal width is 7.8 mm (green color in the colorbar corresponds to -6 dB values of amplitude). The measured focal width of the perfectly focused ellipsoidal lens is 7.9 mm.

(a)

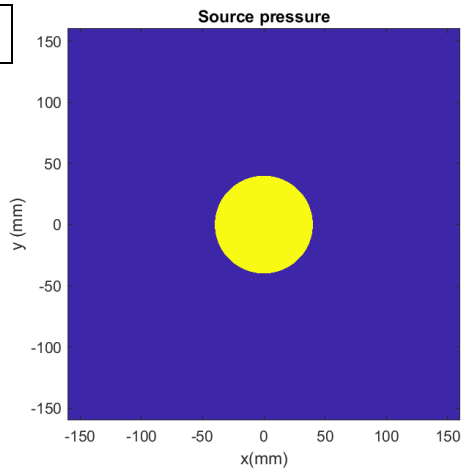
Source pressure
y (mm)
x(mm)

(b)

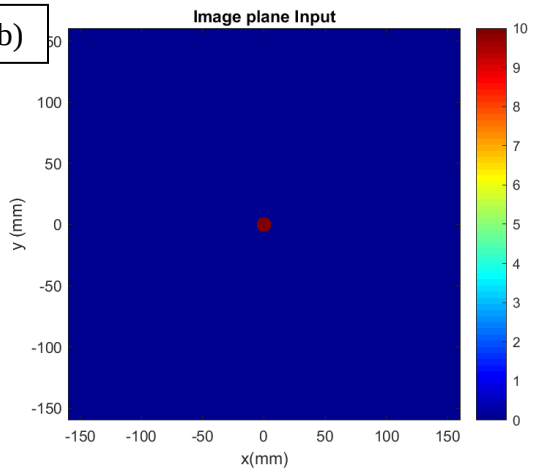
Image plane Input
y (mm)
x(mm)

(c)

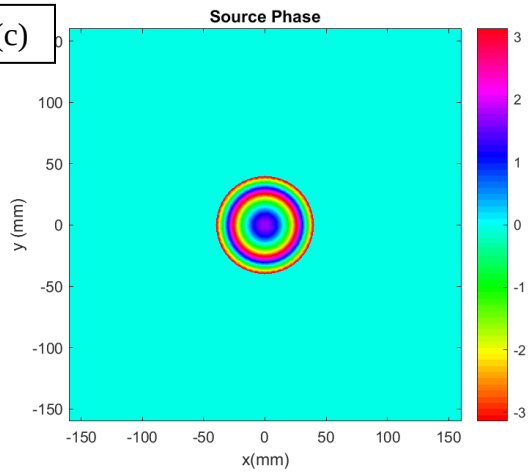
Source Phase
y (mm)
x(mm)

(d)

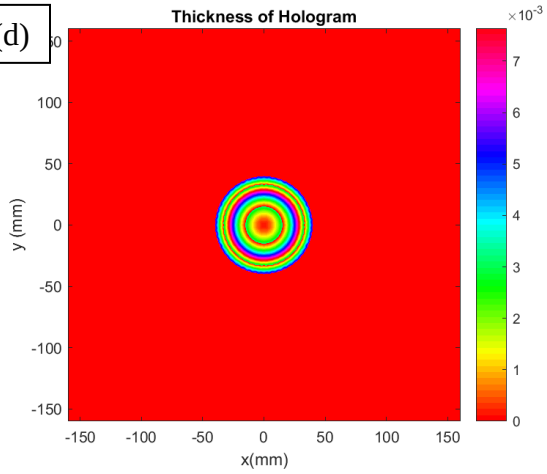
Thickness of Hologram
y (mm)
x(mm)

(e)

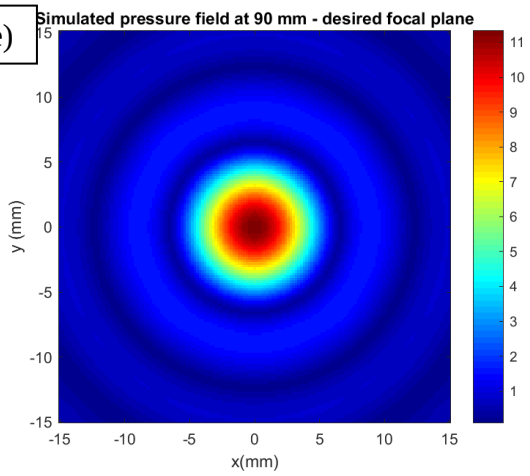
Simulated pressure field at 90 mm - desired focal plane
y (mm)
x(mm)

(f)

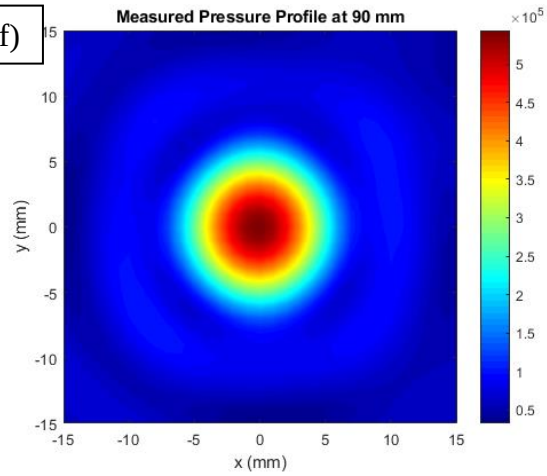
Measured Pressure Profile at 90 mm
y (mm)
x (mm)

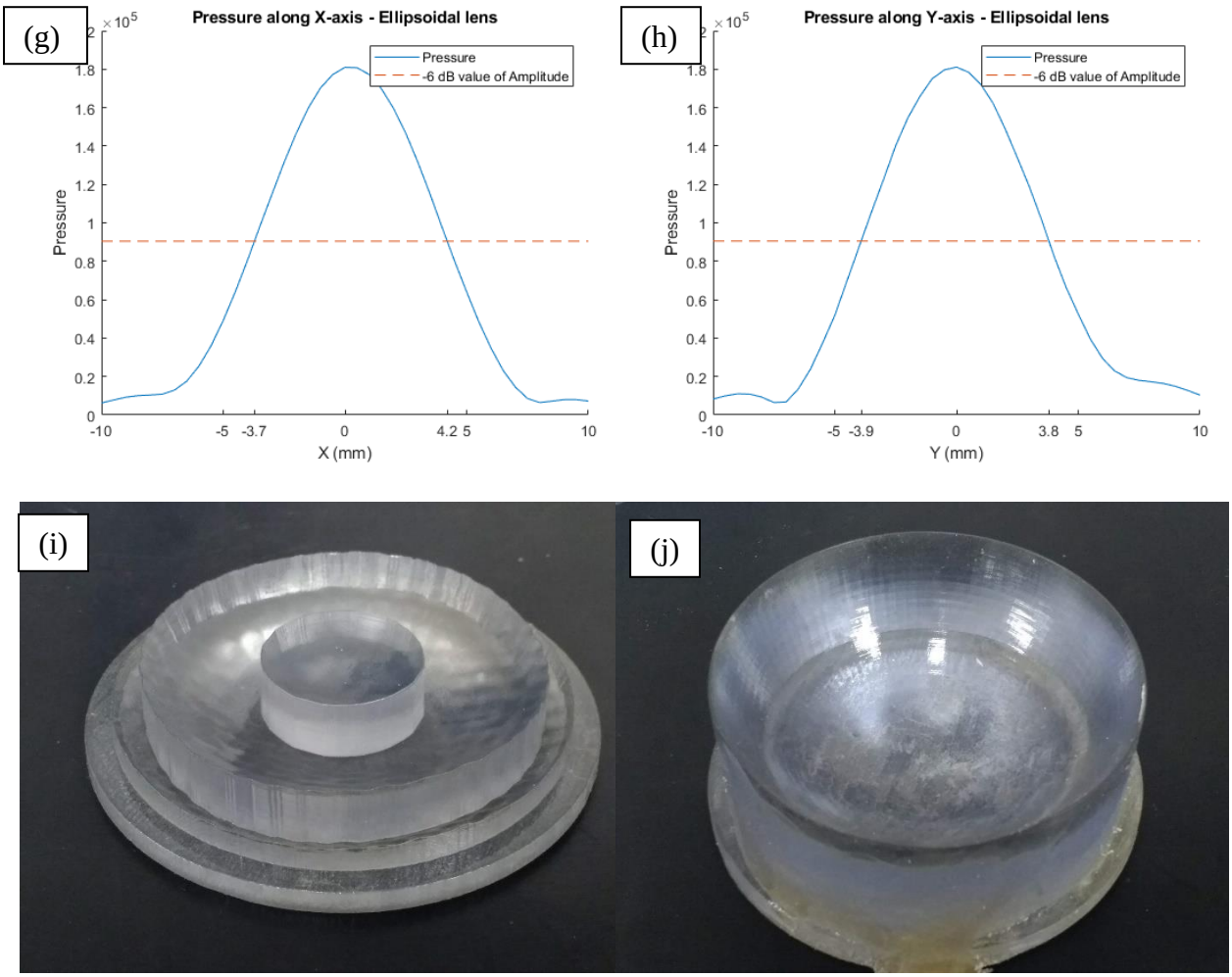

Figure 5.2: The algorithm was validated with a perfectly focusing lens. (a) Source pressure profile (b) The red circle in the center of the image is the desired pressure profile – highly focused beam. (c) Based on the source pressure profile and desired pressure profile in the focal plane, the algorithm calculated required phase distribution at the source. The image shows how phase is distributed for the focused transducer. (d) The required phase distribution at the source is achieved by building a lens with thickness required for introducing sufficient phase change. (e) This image shows simulated pressure profile in focal plane. Please note that green color in the colorbar corresponds to pressure level where it drops to half of the highest-pressure amplitude. (f) This is measured pressure profile. It closely matches with simulated pressure profile. (g) Pressure along X-axis in focal plane of ellipsoidal lens are plotted in the graph. The -6 dB points are located at -3.7 mm and 4.2 mm from the center of the lens. (h) Pressure along Y-axis in focal plane of ellipsoidal lens are plotted in the graph. The -6 dB points are located at -3.9 mm and 3.8 mm from the center of the lens. (i) Lens designed with algorithm and (j) standard ellipsoidal lens with d = 90 mm.

An equivalent Fresnel lens was designed and fabricated with N = 4 in eq. (4), (5) and (6). Its pressure profile was scanned to compare its results with the holographic lens. (The lens is shown in Figure 5.1 (a)). When compared with spherical or ellipsoidal lenses, these thin lenses reduce attenuation of sound wave in the lens. The results of scan of Y-axis in focal plane are shown in Figure 5.3. The results show that the focal width is 8.5 mm.

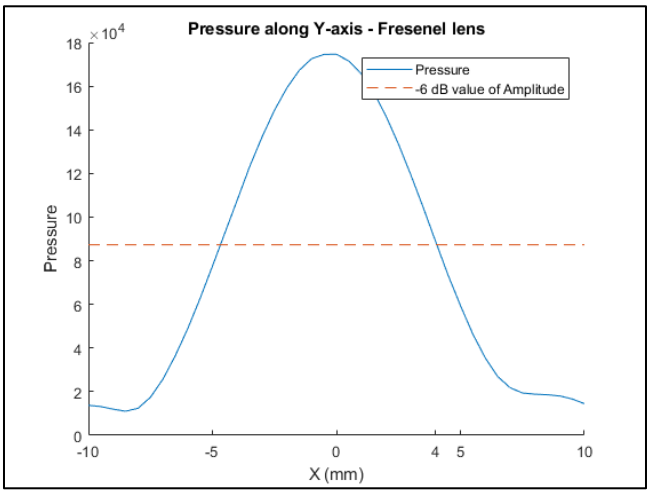

Figure 5.3: Pressure field of Fresnel lens was scanned in focal plane along Y-axis. The focal width is 8.5 mm.

5.4.2 Validation with complex Image

To validate the implementation further with an arbitrary image, desired the pressure profile was set to an image of a husky dog and frequency was set to 1 MHz to achieve higher resolution. A binarized image was set as input to the algorithm, a lens was fabricated, and the pressure profile was scanned to confirm the simulations. The results are shown in Figure 5.4.

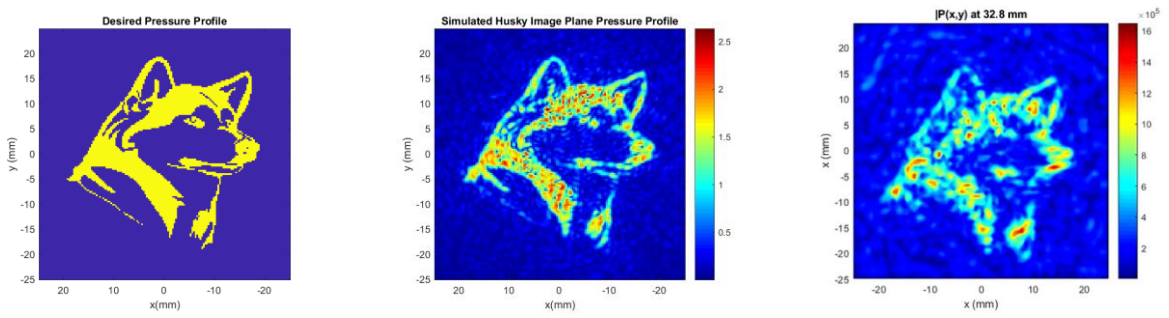

Figure 5.4: Implementation of the algorithm was confirmed with an image of a husky dog (Left to right)t) Desired image, simulated pressure profile and measured pressure profile

5.5 Discussion

Iterative angular spectrum approach is useful for designing arbitrary beam shapes and focus as opposed to conventional perfectly focusing lenses. The algorithm used for designing the lens is simple to implement in a scientific computing application. The output of the algorithm gives thickness of the lens at each point in source pressure profile. The resulting lens is phase wrapped and hence it thickness is limited to thickness required for introducing phase shift of 2π in the wavefront travelling in given pair of media. The results show that the size of the focus produced by the perfectly focusing holographic lens and spherical lens are almost same with difference less than 1.5%. When thickness of a perfectly focusing lens produced by the algorithm was compared with the thickness of the equivalent spherical lens in section 5.4.1, the holographic lens is 3 times thinner than the spherical lens. Reduction in thickness reduces the distance travelled by wavefront in the lens material and incurs less attenuation. However, this phase wrapping necessitates to have certain number of cycles of sine wave in the pulse signal as the edge waves of the transducer don't reach the focus at the same time as center wave. Hence, one needs to calculate difference in time when each wave reaches desired point in pressure field and ensure that the pulse width is sufficiently longer than the time difference to achieve steady state.

One of the limitations of IASA is that it can not produce target image feature which are comparable to wavelength in the medium in which the target is located. Although theoretical limit of diffraction is $\lambda/2$, it was found difficult to produce feature smaller than a wavelength. Hence, the image of the husky was simulated and validated at frequencies higher than 350 kHz.

5.6 Conclusion

IASA is useful for manipulating three dimensional wavefronts. Rapid prototyped lenses produced using IASA can generate complex wavefronts and achieve reconstruction degrees of freedom two orders of the magnitude higher than commercial phased array sources. It scales well to higher information content in the hologram, larger aperture size and higher power. These characteristics are suitable for high intensity ultrasound applications. Hence, this technique was implemented and validated by designing a perfectly focusing holographic lens and its results were compared with an equivalent ellipsoidal lens. The focal beamwidth produced holographic lens is within 1.5% of that of spherical lens. Further, the technique was used to design arbitrary beam shape forming an image of husky dog. The pressure field produced by the lens was scanned and it confirmed the successful implementation of IASA.

References:

[1] A. Marzo, S. A. Seah, B. W. Drinkwater, D. R. Sahoo, B. Long, and S. Subramanian, "Holographic acoustic elements for manipulation of levitated objects," *Nat. Commun.*, vol. 6, no. 1, p. 8661, Dec. 2015.

[2] K. Melde, A. G. Mark, T. Qiu, and P. Fischer, "Holograms for acoustics," *Nature*, vol. 537, no. 7621, pp. 518–522, Sep. 2016.

[3] S. Mellin and G. Nordin, “Limits of scalar diffraction theory and an iterative angular spectrum algorithm for finite aperture diffractive optical element design,” *Opt. Express*, vol. 8, no. 13, p. 705, Jun. 2001.

[4] B. McDonald, “surf2stl - File Exchange - MATLAB Central.” [Online]. Available: https://www.mathworks.com/matlabcentral/fileexchange/4512-surf2stl. [Accessed: 22-Jul-2018].

6 Focus Enlargement with Holographic Lenses

6.1 Introduction

In Ch. 1, we noted that effective and efficient breakage of stones is possible when the size of the focus is larger than the size of the stone, and we have sufficient focal gain to achieve a pressure amplitude of at least 6.5 MPa. We also noted that there are constraints on the geometry and frequency of the transducer. The focal width calculated for the parameters within these constraints (f = 335 kHz, d = 90 mm and $2a$ = 80 mm) is about 7 mm, and the focal gain is 13. As we reduce the surface area of therapy transducer by creating a 4 cm diameter central open in the therapy transducer to fit an imaging transducer, the focal gain drops to 9, and the focal width decreases to 6 mm. However, this focal width is not sufficient to fragment more than 97% of the stones considered for a surgical intervention [1]. Hence, there is a need to develop transducers with different focusing techniques which provide larger focus within the given constraints. This chapter explores whether IASA can generate lenses which produce focus up to 12 mm. The exploration reveals that direct implementation of IASA is not sufficient to enlarge the focus. A few specific modifications need to be made in the desired pressure profile for generating features comparable to wavelength of wave in the medium in which target is located. This chapter details how these modifications were identified and optimized for generating larger focus. Finally, the chapter concludes with experimental results of scans of pressure profile of the most optimized lens.

6.2 Methods to enlarge the focus with IASA

In the last chapter, it was noted that a desired pressure profile in a plane (desired image) is given as input to IASA and it returns phase distribution and thickness of a holographic lens at the source required for producing the lens. This practice was followed to enlarge the focus. The input images had a circle with diameters larger than 6 mm. The diameter of the source profile, focal distance and frequency were set to 85 mm, 90 mm and 335 kHz respectively. However, it was observed that the output of the algorithm converged to a solution similar to desired image having circular shape of diameter 6 mm with no enlargement of the focal width (-6 dB contour). The green color in the colorbar corresponds to values half the highest amplitude in the simulated plane and hence size of the circle in green color roughly estimates size of the focus. The results are shown in Figure 6.1 for d = 10 mm, 12 mm and 16 mm.

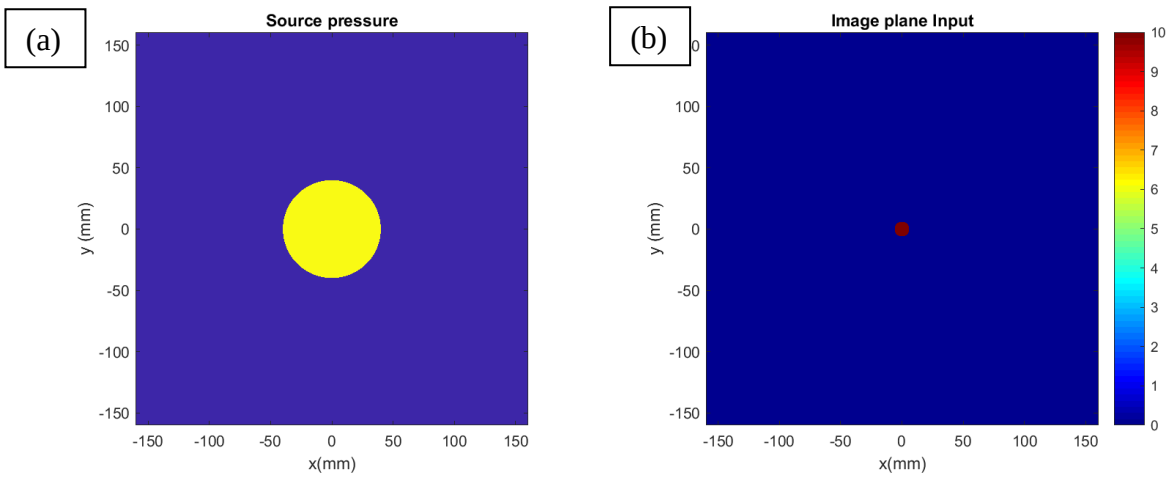

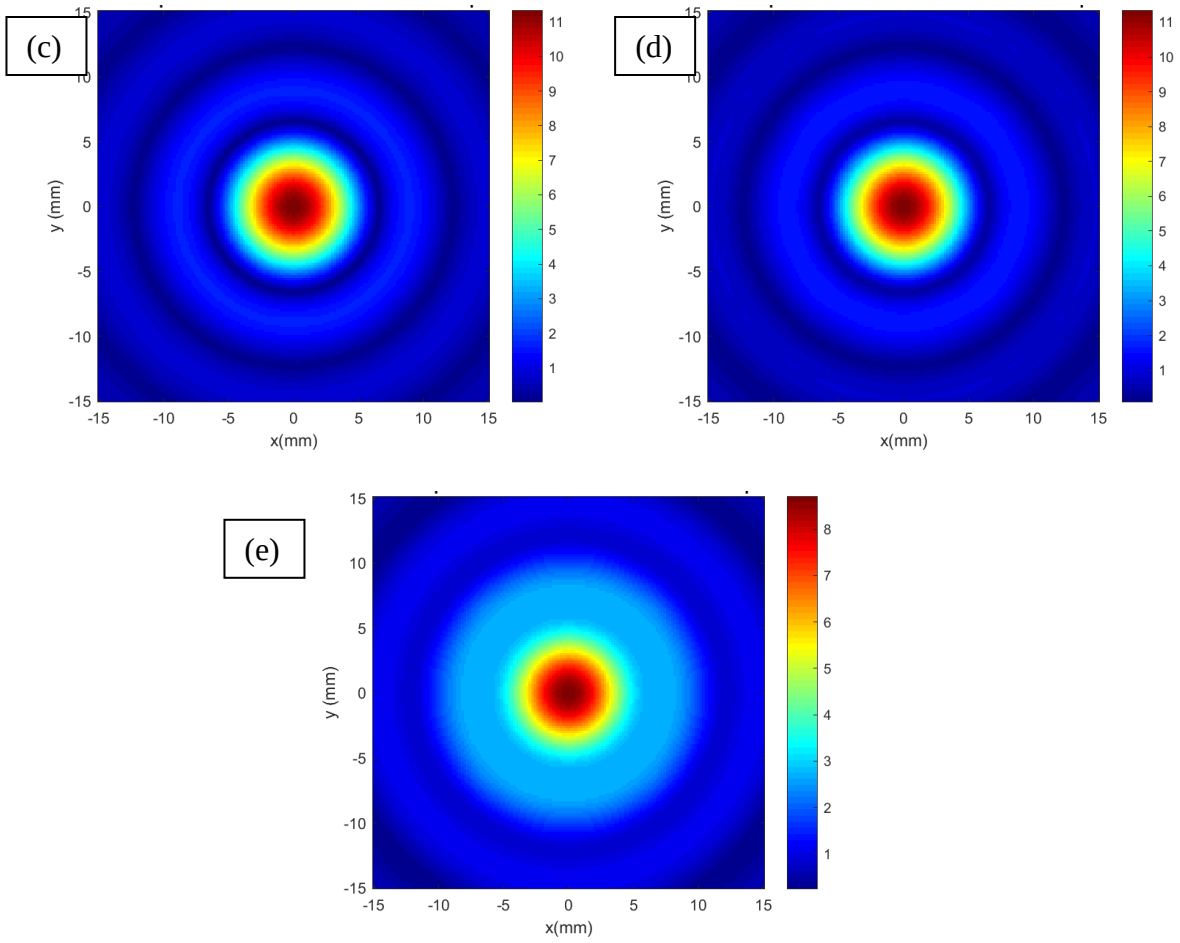

Figure 6.1: (a) Source pressure distribution (b) Desired pressure profile in the focal plane (c) Simulated pressure profiles desired circular shape with diameter D = 10 mm (d) D = 12 mm (e) D = 16 mm. The green color in the colorbar corresponds to values half the highest amplitude in the focal plane. (-6 dB contour). It should be noted that there was no enlargement in focus as diameter of desired circular shape was increased. The IASA failed to produce enlarged focus.

Changes in the simulated pressure profile were observed for diameter greater than 16 mm. However, it was found that the maximum pressure along the z-axis was farther from desired focal plane. The results are shown in Figure 6.2 for diameter 20 mm. The plane located at 15 mm from the desired focal plane has higher maximum pressure than that of desired focal plane.

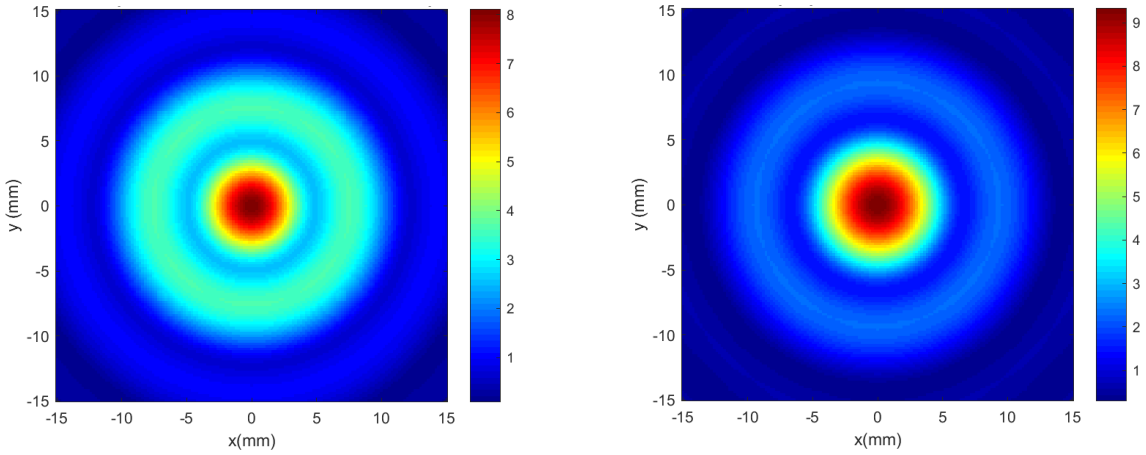

Figure 6.2: When source pressure distribution was same as Figure 6.1 but desired image had diameter larger than 16 mm, the simulated focal plane was different from the simulation in Figure 6.1. This figure shows simulated pressure profiles for image plane having circular shape with 20 mm diameter. The left image is simulated desired pressure profile which has annular ring concentric with focus. However, the desired focal plane doesn't have highest amplitude of pressure in a plane. Its focal gain is 8 while a plane located 15 mm away from focal plane (right) has focal gain 9. Further, the diameter of -6 dB is contour in this plane is 6 mm. Again, the algorithm fails to generate focus up to 20 mm in diameter which is almost 5 times larger than the wavelength (λ = 4.3 mm) at f =335 kHz.

To reduce the maximum pressure in planes outside than the focal plane, we set low pressure values in planes before and after the focal plane. However, simulations with three desired image planes did not converge to a solution with highest maximum pressure in the focal plane. Further, different weighing functions were laid over the circular shape in the desired image plane – concentric circular shapes having different pressure levels. However, these attempts led to solutions similar to results in diameter ranging from 6 mm to 20 mm and focal width didn't increase. It was unclear if these results were due to the diffraction limit or due to discrepancy in the implementation. Hence, these weighted functions were simulated at frequencies higher than 350 kHz. It was found that the output converged to different solutions for frequencies higher than 700 kHz. The simulations are shown in Figure 6.3 for 1000 kHz. As the simulated outputs match closely with desire image, it is confirmed that the algorithm is implemented correctly.

(a)

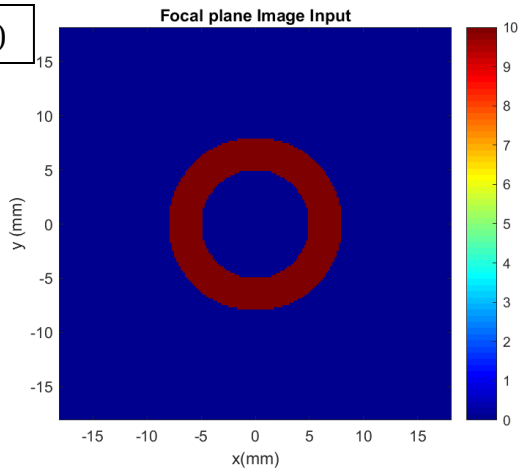
Focal plane Image Input
y (mm)
x(mm)

(b)

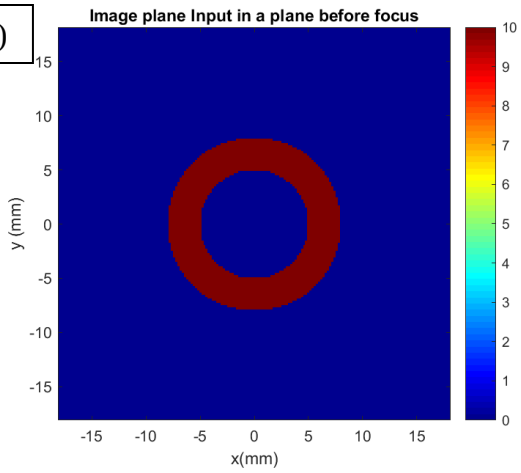
Image plane Input in a plane before focus
y (mm)
x(mm)

(c)

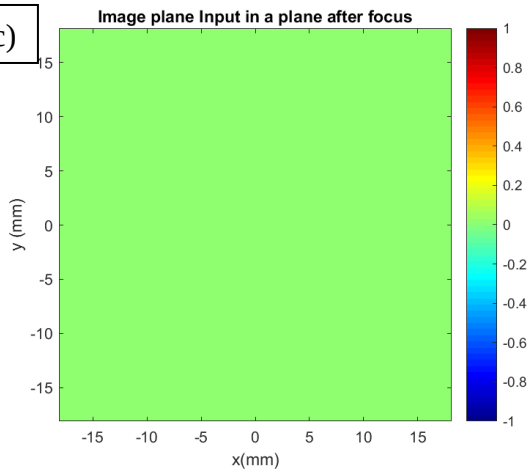
Image plane Input in a plane after focus
y (mm)
x(mm)

(d)

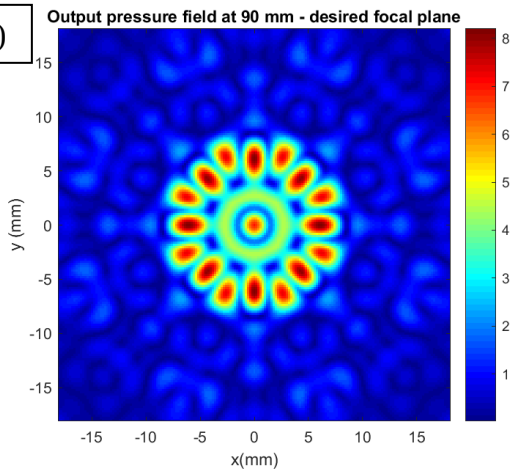
Output pressure field at 90 mm - desired focal plane
y (mm)
x(mm)

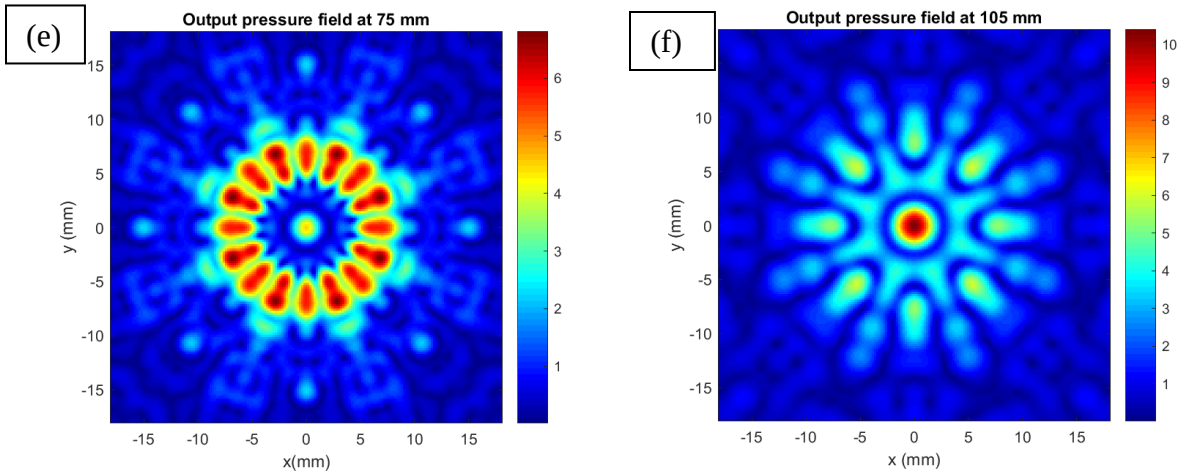

Figure 6.3 An annular ring was set as desired pressure profile in the focal plane to avoid perfect focusing observed in previous simulations. The profile was simulated at various frequencies from 350 kHz to 1500 kHz. It was observed that the output of algorithm closely matched with desired image at frequencies higher than 700kHz. This figure shows simulations at f = 1000 kHz (a) Desired Pressure Profile in the focal plane (b) Desired image in a plane 15 mm before the focal plane (c) Desired pressure profile in a plane 15 mm after the focal plane (d) Simulated pressure field in desired focal plane d = 90 mm (e) Simulated pressure field in a plane 15 mm before focal plane (f) Simulated pressure profile in a plane 15 mm after the focal plane. Although desired pressure profile was obtained in the focal plane, the beam appeared to form a perfect focus in a plane away from desired focal plane. Again, it should be noted that the highest maximum pressure was observed in this new plane away from the focal plane.

Whereas the same desired pressure profiles at 600 kHz produced results shown in Figure 6.4.

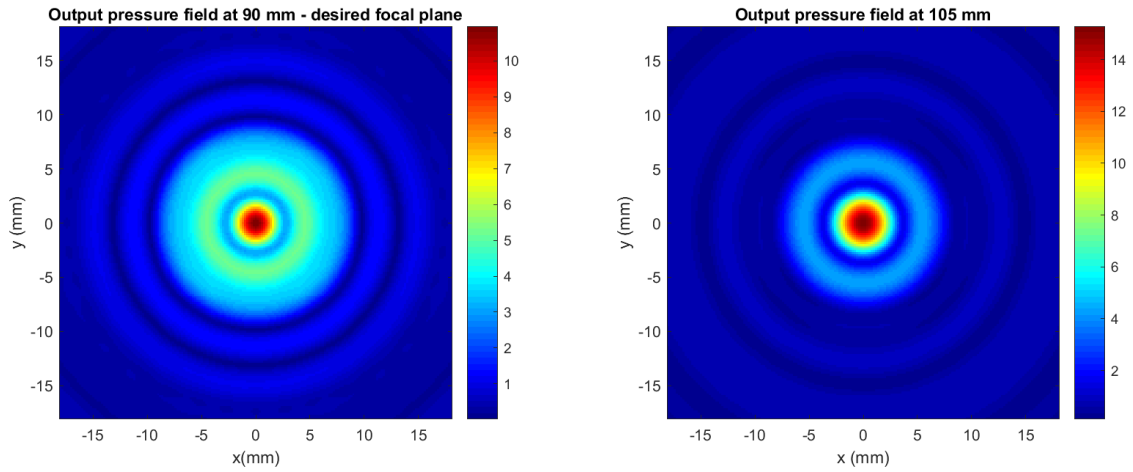

Figure 6.4: If desired images (a), (b) and (c) from Figure 6.3 are simulated at f = 600 kHz instead of f = 1000 kHz, it converges to a solution similar to focused lens case (left). Highest maximum pressure in a plane is observed in a plane 15 mm after the focal plane (right). Again, the algorithm fails to generate annular shaped ring at lower frequencies even though dimensions are with diffraction limit.

Finally, asymmetry was introduced in the desired pressure profile to explore the possibility of algorithm converging to a different solution. The center of the circle in desired image plane was shifted to (p mm, p mm) where p varied from 0 to 9 in steps of 1 mm. The diameter of desired pressure profile was varied from 8 mm to 20 mm in steps of 2 mm. The frequency of the transducer was 335 kHz and the source pressure profile was adjusted to accommodate an imaging transducer at the center. The simulations are show in Figure 6.5 for desired circular shape with diameter 18 mm, its center was shifted to (4 mm, 4 mm) and focal distance was 90 mm.

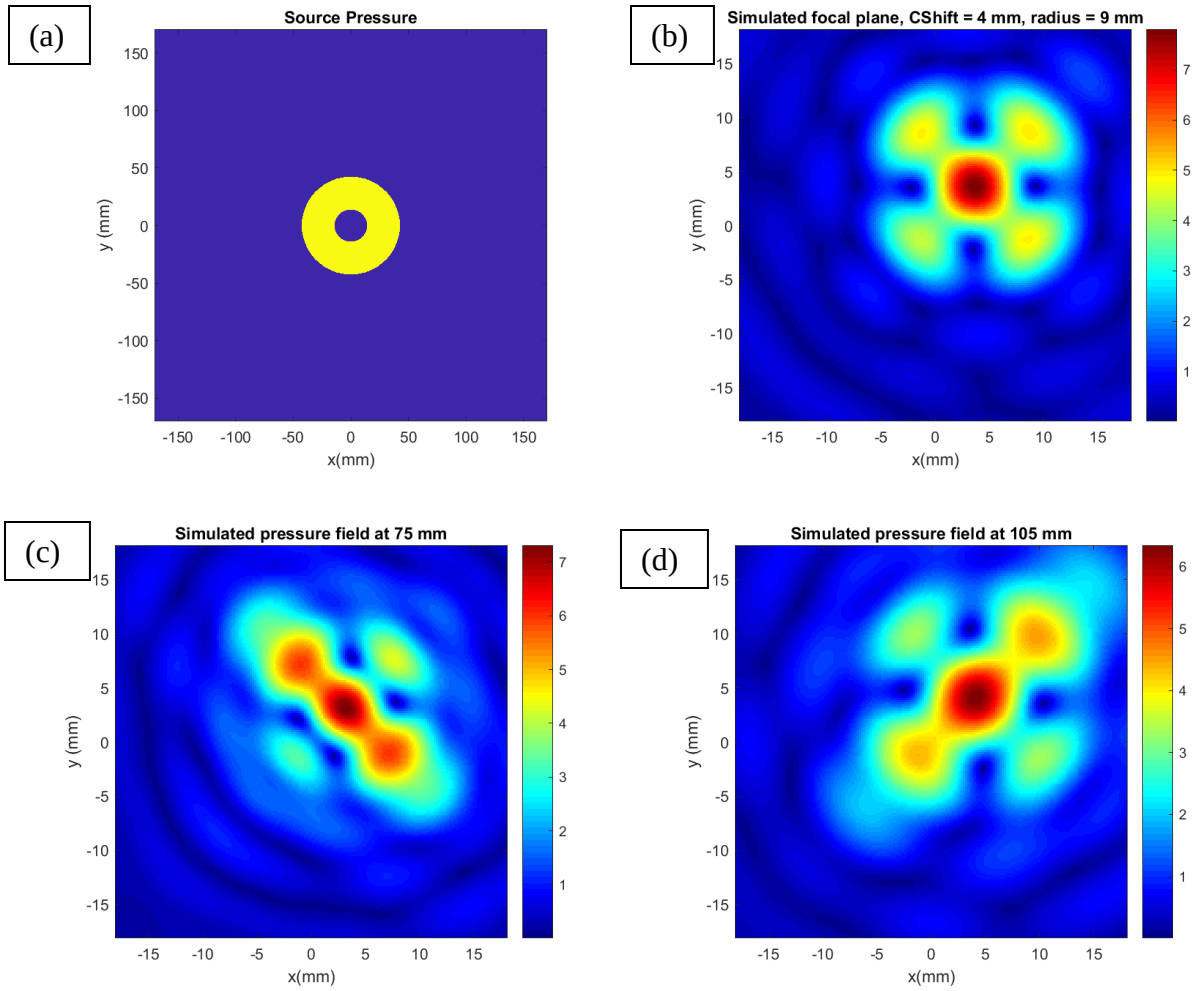

Figure 6.5 Asymmetry in desired image plane to explore possibility of convergence to a different solution. The center of desired circular shape of 18 mm diameter was shifted from (0 mm, 0 mm) to (4 mm, 4 mm). The image plane was located at 90 mm from transducer plane and r f = 335 kHz. (a) Source pressure profile (b) Simulated pressure profile of focal plane (c) Simulated pressure profile 15 mm before focal plane (d) Simulated pressure profile 15 mm after focal plane. It should be noted that the highest-pressure amplitude is in the desired focal plane. Thus, introducing asymmetry in the desired focal plane or source pressure profile was found to generate solutions different from previous simulations having circular shapes of the same size.

It can be seen that introducing asymmetry leads convergence to different solutions even for frequencies below 600 kHz. The size of the -6 dB contours is large and farthest points are 18 mm away. Also, the highest-pressure amplitude is located in desired focal plane. To optimize the results

further we drew inspiration from these simulations and simulations of the ring-shaped profile at 1000 kHz. The shape of desired pressure profile was set similar to image shown in Figure 6.6.

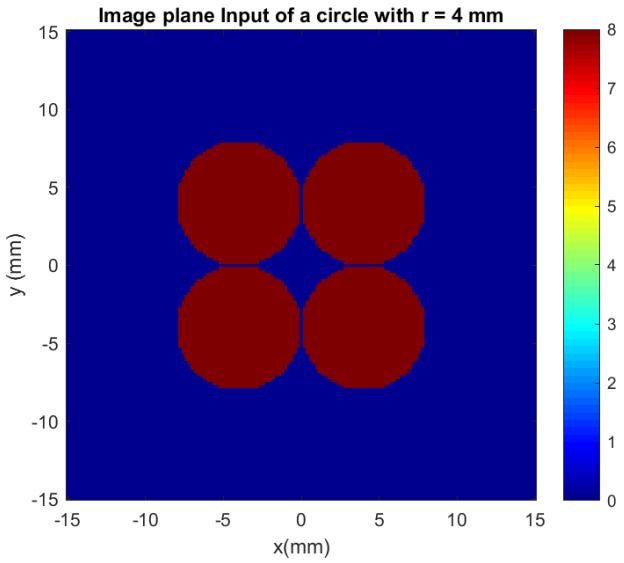

Figure 6.6: Desired pressure profile - inspired from red regions and yellow regions in simulated focal planes in Figure 6.3 (d) and Figure 6.5 (b) respectively. Centers of circles are located at (±4 mm, ±4 mm) and diameter of a circle is 6 mm.

Variations in diameter of each small circle from 4 mm to 8 mm in step size of 1 mm were simulated. Further, the location of the centers of circles was varied from (±0, ±0) to (±8, ±8) in step size of (1,1). These desired pressure profiles were simulated at 300 kHz, 335 kHz, 350 kHz and 400 kHz. The center of the source pressure profile was also varied from (0,0) to (8,8). Effect changing locations of centers of circles in desired image plane can be seen in Figure 6.7. The source profile was same as in Figure 8 (a) but its center was shifted to (1 mm, 1 mm) to introduce asymmetry. The results are simulated for 335 kHz.

(a)

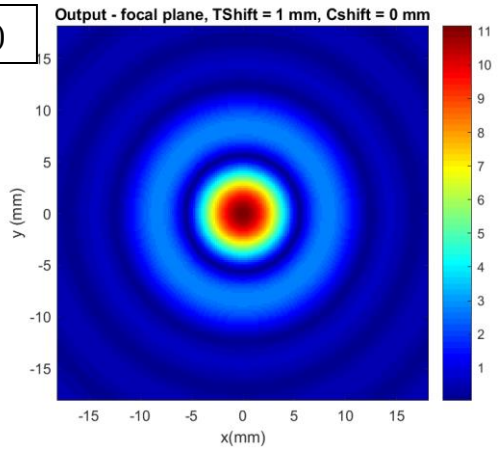
Output - focal plane, TShift = 1 mm, Cshift = 0 mm
y (mm)
x(mm)

(b)

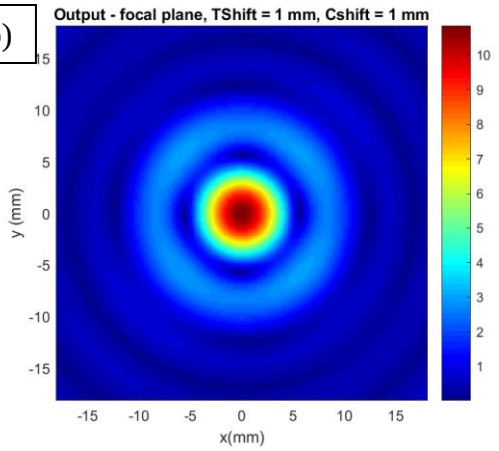
Output - focal plane, TShift = 1 mm, Cshift = 1 mm
y (mm)
x(mm)

(c)

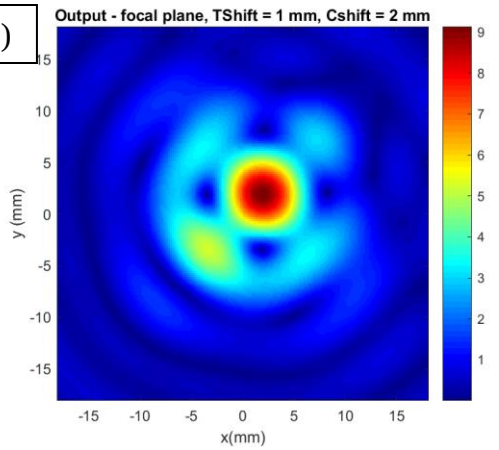
Output - focal plane, TShift = 1 mm, Cshift = 2 mm
y (mm)
x(mm)

(d)

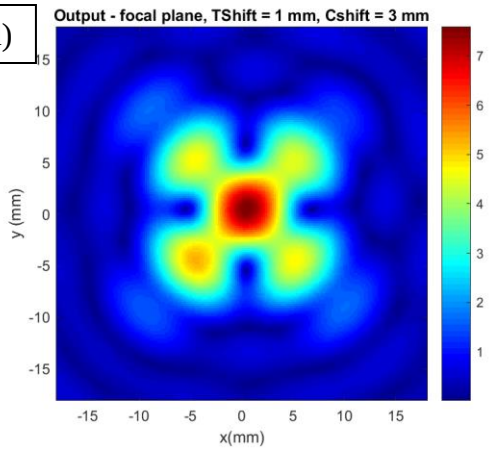
Output - focal plane, TShift = 1 mm, Cshift = 3 mm
y (mm)
x(mm)

(e)

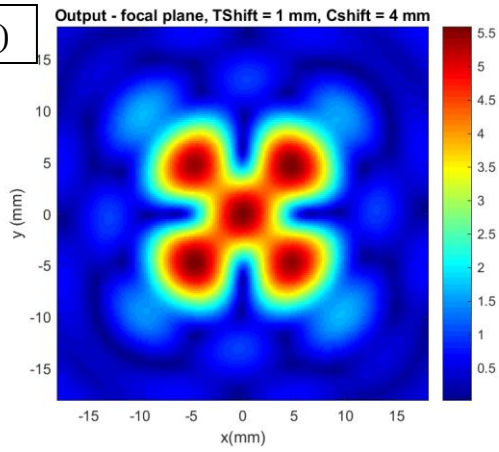
Output - focal plane, TShift = 1 mm, Cshift = 4 mm
y (mm)
x(mm)

(f)

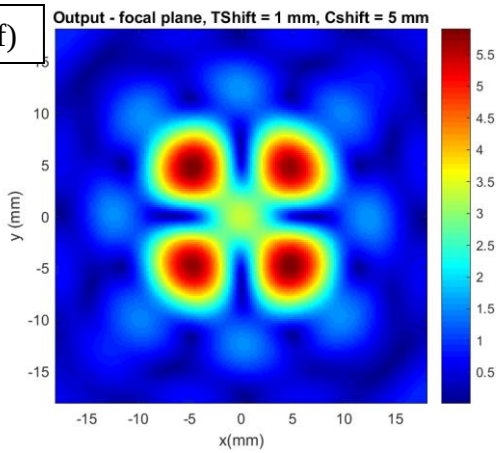
Output - focal plane, TShift = 1 mm, Cshift = 5 mm
y (mm)
x(mm)

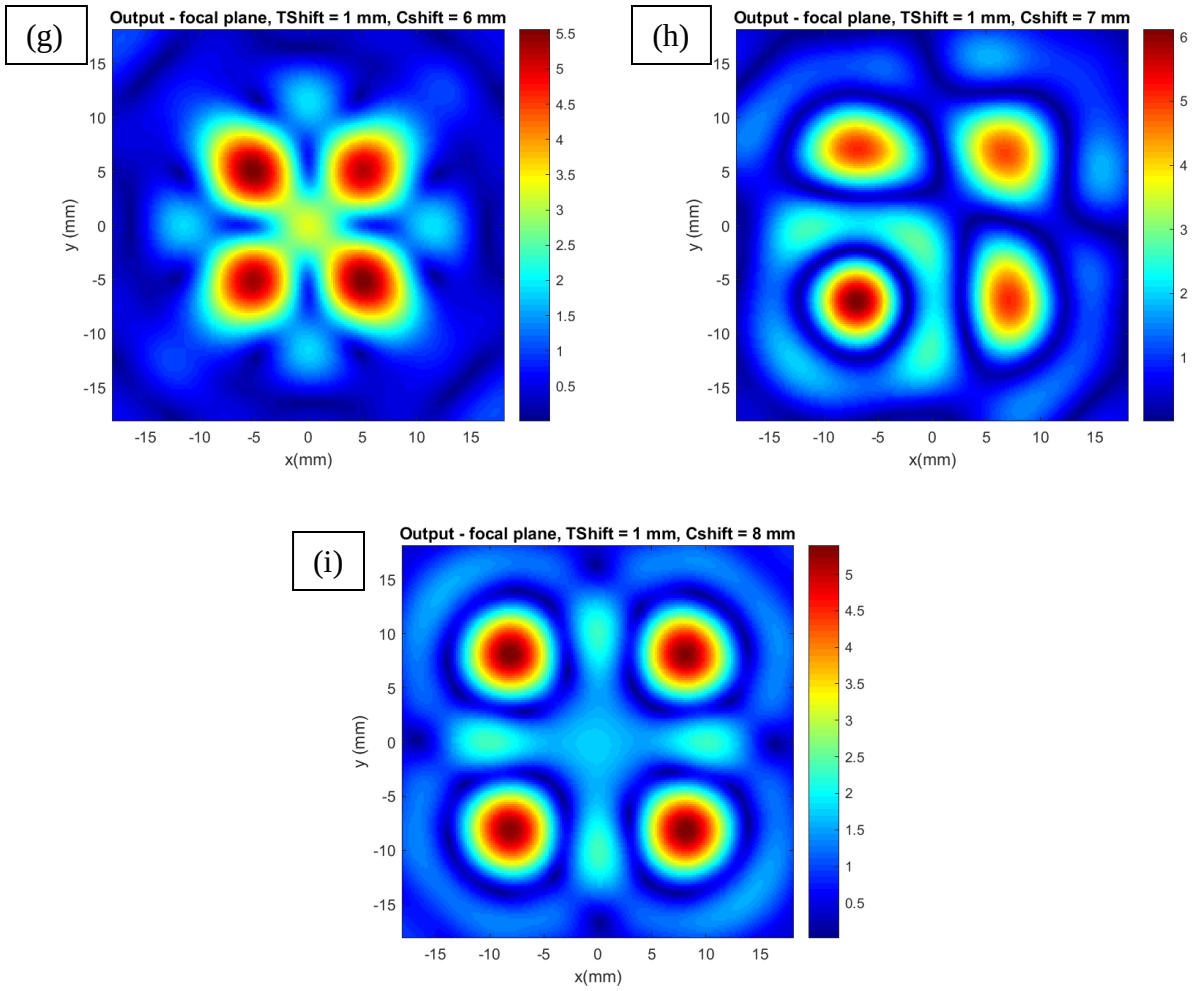

Figure 6.7: If the locations of centers of the circles in Figure 6.6 are changed from (0 mm, 0 mm) to (±8 mm, ±8 mm) in step size of (1 mm, 1 mm). The simulated pressure profiles in the focal plane are shown for each shift. The title of each graph conveys that the simulated plane is the desired focal plane. Tshift values in the title convey that the center of the circle of the source profile was shifted to (1,1) mm while Cshift values help to locate the centers of the circles in the desired pressure profile. The centers of these circles were located at (±p mm, ±p mm) for Cshift = p. The focal plane was located at 90 mm from the transducer plane (f = 335 kHz). The source profile was same as in Figure 8 (a) but its center was shifted to (1 mm, 1 mm) to introduce asymmetry.

The patterns had similar trends for the variation in other parameters at different frequencies. There was an exception to this pattern when it was simulated at 300 kHz for circles located (±4 mm, ±4 mm) and center of the source profile was shifted to (p mm, p mm) where p varied from 1 to 5. The simulated focal plane is shown in Figure 6.8 for p = 3. Inner and outer diameters of the source

profile were 28 mm and 85 mm respectively. This pressure profile has a minimum at the center but has uniform pressure amplitude outside it. Size of minimum is 2.5 mm (-6 dB contour) whereas length of outer -6 dB contour is 14 mm. This pressure profile can be useful for fragmenting stones larger than 6 mm into pieces smaller than 2.5 mm. Efforts were made to generate similar pressure profiles 335 kHz, 350 kHz and 400 kHz by studying relation between frequency, focal distance and size of the focus. The focal distance was varied from 78 mm to 105 mm in step size of 3 mm.

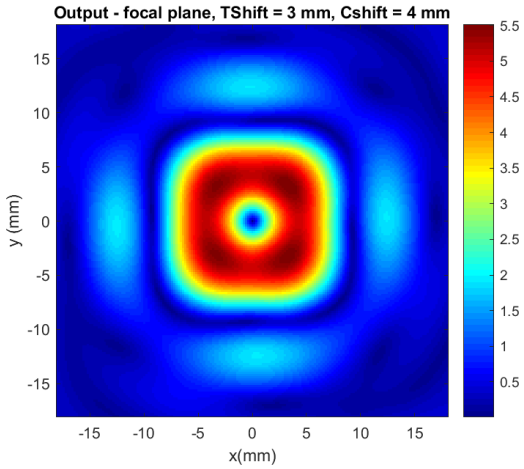

Figure 6.8: Simulated pressure profile in a focal plane (d = 90 mm and f = 300 kHz) for desired image similar to Figure 6.6. The centers of the desired circular shapes were located at (±4 mm, ±4 mm) and their diameter was 6 mm. The source profile was similar to as shown in Figure 6.5 (a) but its inner and outer diameter were 28 mm and 85 mm respectively. The center of source profile was shifted to (3 mm,3 mm). This profile is different from the all the simulated profiles in the Figure 6.7. The size of the -6 dB contour was 12 mm. But there was a minimum at the center with 2 mm diameter.

6.3 Annular pressure profile for fragmenting larger stones

It was found that the annular pressure profile with focal width of 12 mm can be achieved at 350 kHz with focal gain of 5.5 at focal distance of 84 mm. The center of the source profile is located at (3.5 mm, 3.5 mm), center of circles in the image in desired plane are located at (±3 mm, ±3 mm) and their diameter is 6 mm. Inner and outer diameters of source profile are 36 mm and 80 mm

respectively. This inner diameter ensures that we integrate GE M5Sc probe for imaging and stone detection. A lens was fabricated based on the thickness matrix and scanned for confirming the results. Figure 6.9 shows simulated and measured pressure profiles in focal plane. The difference in simulated focal width and that measured by hydrophone is ≤1 mm, and the structural-similarity index value is greater than 0.65. The differences in structures are due not to shape and size of the -6 dB contours but to amplitude distribution within the contour.

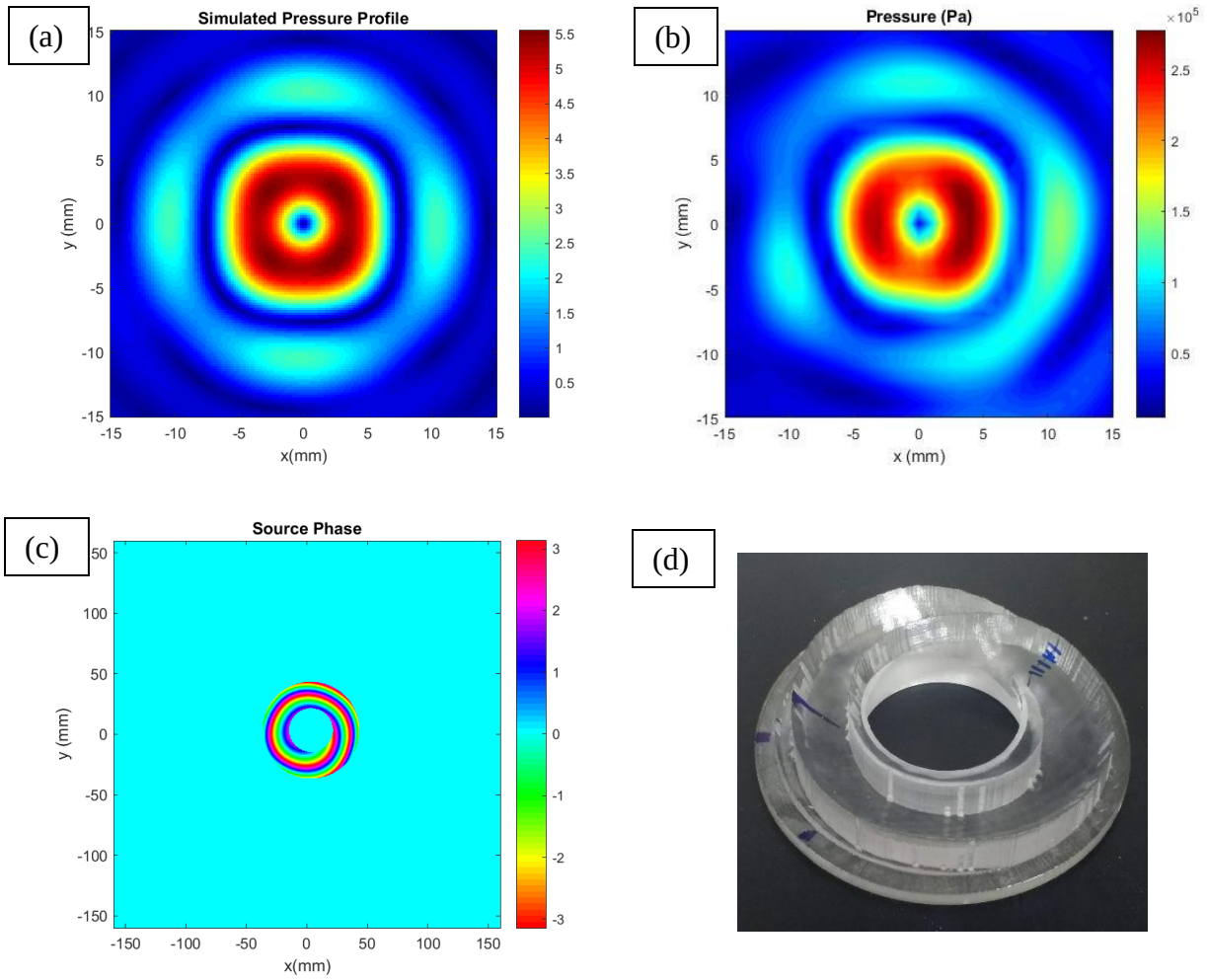

Figure 6.9: (a) Simulated pressure profile in a focal plane located d = 84 mm (f = 350 kHz). The desired image had shape similar to Figure 6.6 but the centers of the circles were located at (±3 mm, ±3 mm). The source profile was similar to as shown in Figure 6.5 (a) but its inner and outer diameter were 36 mm and 80 mm respectively. The center of source profile was shifted to (3.5 mm, 3.5 mm). (b) The measured pressure profile (c) Source phase (d) fabricated lens.

6.4 Discussion

To enlarge the focus, designing acoustic lenses with holography gives great flexibility in designing various beam shapes. However, as the features in desired image have dimensions comparable to the length five times of wavelength, the pressure field was formed with circular shaped dots where

the diameter (-6 dB contour) of these circular shapes was about one wavelength and distance between these two dots is also a wavelength. When dimensions of feature in desired image were comparable to wavelength, it was very likely that the algorithm would converge to a solution which may not match with desired image. If the desired focal plane image was symmetric about origin, the desired focal plane (the plane at desired focal distance) may not have highest amplitude of pressure. The highest amplitude of pressure was located in a plane distal from the focal plane in the direction of propagation. To avoid this shift of focus in direction of propagation, introducing asymmetry in the image plane or transducer plane changed the results drastically. However, it was difficult to predict if these changes produce desired pressure field. If these changes resulted in a pressure field that closely matches with desired pressure field, there was no structured way to find out optimal solution. In this case of enlargement of the focus, the optimal solution was found out by simulating as many different possibilities as possible and the simulations were analyzed visually. The Figure 6.9 shows the most optimal solution found by these simulations. The measured output closely matches with simulation but it was slightly distorted. These distortions may be due to the fact that the shape in the focal plane was not symmetric about axis of the transducer in the direction of propagation and the region near the axis had higher focal gain.

An alternative method for analysis was studied by analyzing diagonal entries in the simulated pressure profile matrix, however no trend was observed to correlate these entries with the optimal solution. Hence, there is a need to develop an analysis tool which can more accurately compare desired pressure field and simulated pressure field. Also, future work can be focused on developing weight functions for images having features comparable to wavelength or symmetric about origin so that optimal solutions are obtained. It should be noted that as we increase size of the focus, focal

gain drops. To maintain high pressure at the focus, one needs to have PZT material which can generate high surface pressures as compared to currently used PZT4 elements.

6.5 Conclusion

An algorithm for developing acoustic holograms using a lens was implement and confirmed by generating a perfectly focused lens and an image of husky dog. We used technique to generate focus twice the size of the perfectly focused lens, however the algorithm converged to a solution producing focal length same as focused lens. By introducing asymmetry in the desired image, we were able to obtain different solutions and produce a pressure fields with larger focus. For f = 335 kHz, d = 84 mm and 2a = 80 mm, we were able to produce a 12-mm wide focus with a minimum of 2.5-mm in diameter at the center. We fabricated the lens and confirmed these simulations by scanning the pressure field. The difference in simulated focal width and that measured by hydrophone was ≤1 mm, and the structural-similarity index value was greater than 0.65. The differences in structures are due not to shape and size of the -6 dB contours but to amplitude distribution within the contour.

References:

[1] Tiselius, Hans-Göran, and Annika Andersson. "Stone burden in an average Swedish population of stone formers requiring active stone removal: how can the stone size be estimated in the clinical routine?." *European urology* 43.3 (2003): 275-281.

7 Fabrication and Testing of a BWL Transducer with Enlarged Focus

Ch.1-7 discuss why we need a BWL transducer with enlarged focus (with focal beamwidth ~ 12 mm) and how different components of a BWL transducer can be modified to achieve it within given constraints. This chapter describes how a BWL transducer was designed and fabricated with the lens producing broader focus. The transducer was characterized by scanning pressure field in the focal plane and determining maximum pressure output at the focus. This chapter concludes the thesis with an experiment comparing efficacy of the new transducer to a narrow focus equivalent for fragmenting large artificial stones (6 mm diameter and 11 mm length) with the transducer.

Before getting into details of design of each component of the transducer, revisiting discussion in Ch.1 will be helpful to understand the requirements clearly. The transducer must have the following characteristics:

- A broad focus (up to 12 mm).
- Peak focal pressure about 6.5 MPa.
- A focal distance of 80 to 90 mm based on skin-to-stone distance and room to maneuver the transducer.
- An aperture of 80 mm based on the available acoustic window.
- An ultrasound imaging probe needs to be incorporated at the center of transducer for image guidance. A circular cutout of 40 mm in diameter is sufficient for assembling the GE M5Sc probe in the transducer.

- The frequency of the transducer should be greater than 285 kHz to break stones into fragments smaller than 2 mm.

7.1 Design of transducer with enlarged focus

In this section, modeling and designing of different components except acoustic lenses are described. The acoustic lens designed in section 6.3 of Ch. 6 is used for fabricating the transducer.

7.1.1 PZT elements

PZT material should be chosen such that it can produce required surface pressure. From the last simulations of the annular pressure profile in section 6.3, the expected focal gain with the lens is G = 5.5. To achieve a focal pressure of 6.5 MPa, we need a surface pressure amplitude of 1.2 MPa. Based on the data of failure tests of PZ36 elements in Ch. 4, it is known that surface pressure of 1.4 MPa can be achieved by applying about 2600 V (peak-to-peak) across the elements. Hence, PZ36 was chosen as piezoceramic material for generation of the pressure waves. Further, when a 25 mm × 25 mm × 4.2 mm element was coupled with a lens (made of Veroclear®) using a matching layer (Z = 7 MRayls and 2.2 mm thick), input electrical impedance was 364 Ω with phase angle of -71.4° at 350 kHz. The matching network was designed to get real impedance of 17 Ω at 350 kHz. When voltage across the element is about 2600 V and, the average electric power is 1506 W. (eq. 13). Hence the average electric intensity is 241 W/cm^2 (calculated by dividing power by area of the transducer).

PZ36 elements were commercially available as square plates with side length of 70 mm. These elements need to be cut in sectors to make annular ring-shaped transducer (inner diameter = 40 mm and outer diameter = 80 mm). The total number of sectors was chosen based on the impedance

of the element with matching network. The following table shows how impedance of the required matching network varies with number of segments.

Table 3 Possible Element Configurations for a broadly focused transducer

Area of annular ring in cm^2	Number of Sectors	(area of a sector) – (area of supporting structure) cm^2	Required electrical power for a sector in W (Electrical Intensity X Area of a sector)	Input voltage from the Amplifier in V (peak-to-peak)	Desired Impedance of combination of matching network and PZT element in Ω (Eq. 13)
37.7	3	11.8	2843.8	320	9.02
37.7	4	8.6	2072.6	320	12.35
37.7	6	5.5	1325.5	320	19.31

It should be noted that each element rests on a supporting structure which is part of housing (shown in Figure 7.1). These structures take up some area (in this case 0.8 cm^2 for each sector) from the radiating surface and hence it is subtracted from the actual area of a sector. Four sectors were chosen for further development as the required impedance was within the range 10-20 Ω. Although PZT elements in six sector design had impedance within the same range, four sectors were chosen to reduce loss in radiating surface.

7.1.2 Matching layer

Acoustic impedance of PZ36 is 18 MRayls and that of the lens material is 3 MRayls. Required acoustic impedance of matching layer is 7 MRayls as per eq. 16. This impedance was achieved by a composite made from white aluminum oxide (grit #600) with epoxy. The composite had 73% aluminum oxide by weight and sound speed of 3043 m/s. However, the composite material was too viscous to spread uniformly on the surface of the PZT. Hence, new composite with 70% aluminum oxide by weight and acoustic impedance of 6.8 MRayls was prepared. The sound speed

in the new composite was 2965 m/s and associated wavelength at 350 kHz was 8.47 mm. Hence, nominal thickness of the matching layer was $\lambda_{matching}/4$ = 2.12 mm. In the final design of the transducer, thickness of the transducer was designed to be 2.2 mm, within the thickness variation tolerance of $\pm \lambda_{matching}/30$.

7.1.3 Housing and fabrication

All 4 sectors of the PZ36 elements, matching layer and the lens are held together by a housing as shown in Figure 7.1 The housing was designed such that it supported all the PZT elements, but area of contract between the housing and elements was minimized to avoid acoustic losses in the direction of housing support. The composite of matching layer was spread on the surface of PZT elements and the lens was clamped on it. Geometric constraints between the housing and the lens ensure that the thickness of the matching layer was 2.2 mm. Vents were designed for free flow of extra composite material. All the elements were backed with a low-density but rigid polyurethane foam. Finally, all the joints were sealed with a room temperature vulcanizing silicone rubber having high dielectric constant. The matching layer and silicone rubber were allowed to cure for 24 hours.

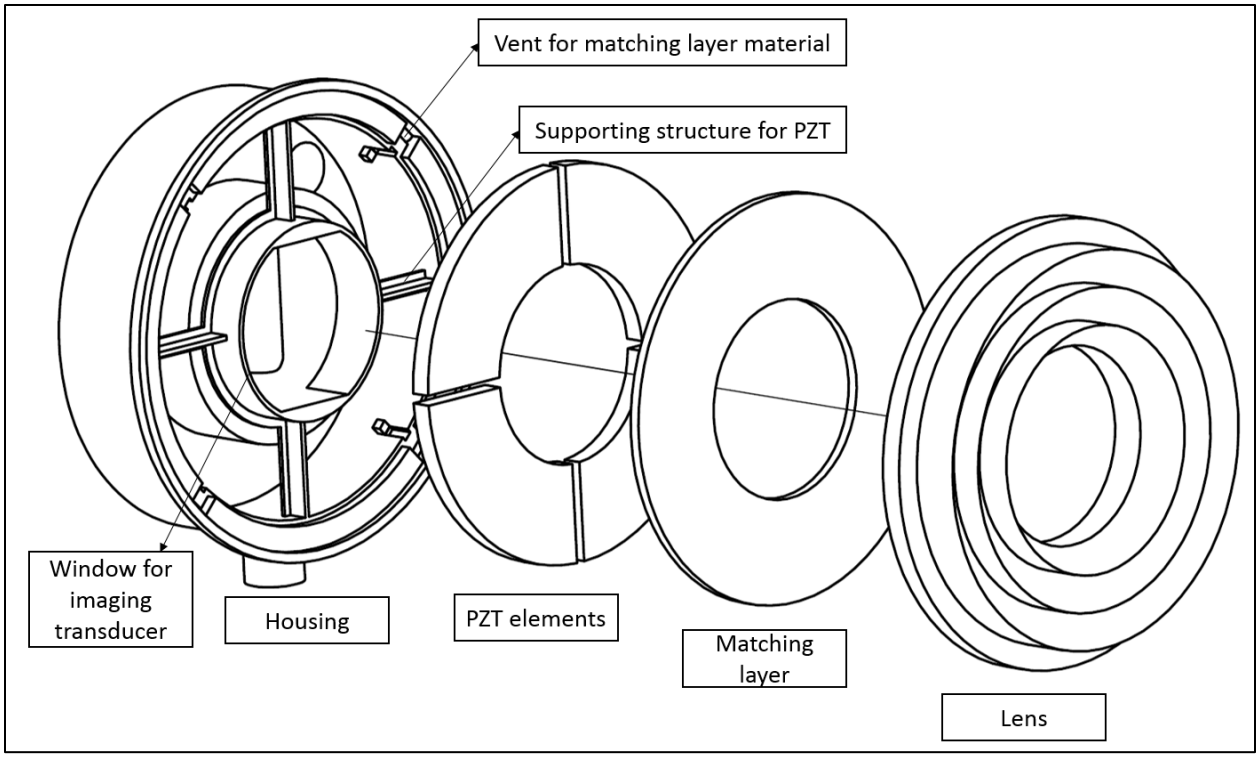

Figure 7.1 Exploded view of the transducer. The transducer holds four sectors of PZ36. A matching layer is spread over the PZ36 sectors. Finally, a lens clamped on top of the matching layer. Geometric constraints between housing and lens ensure required thickness of matching layer.

7.1.4 Matching network

Once the transducer was fabricated, the impedance vs. frequency response of the transducer was analyzed with impedance/antenna analyzer (AIM 4300, Array Solutions, Sunnyvale, TX). Each element was matched to real impedance of 10 Ω. Measured impedances varied between 9 and 11 ohms with phase angles between ±12°. Electric impedance vs. frequency plot for an element is shown in Figure 7.2.

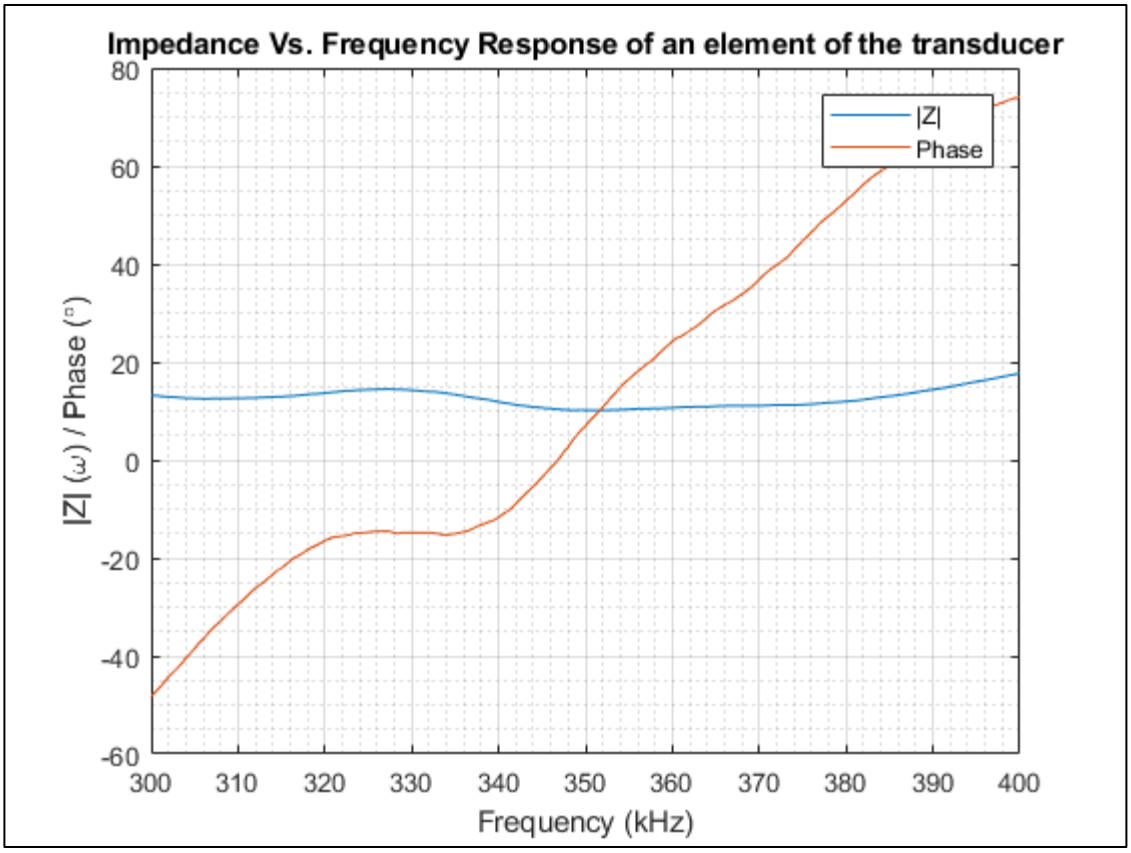

Figure 7.2 Electrical Impedance vs. Frequency response for all the elements were analyzed and the elements were matched to 10 Ω at 350 kHz with L-bridge step down network. Here, the element is matched with a frequency smaller than 350 kHz and magnitude and phase of 10.2 Ω and 7° respectively at the resonance frequency. When wires used in analyzing the circuit are removed in the final operation, inductance of the circuit decreases, and the element is perfectly matched to 350 kHz.

7.1.5 Characterization of the transducer

To confirm the shape of the focus in the focal plane, the transducer was characterized by measuring pressure amplitude in focal plane. First, a 2D plane was scanned at 84 mm (designed focal distance) from the surface of the transducer with a low-pressure hydrophone (HNR-0500, Onda, Sunnyvale, CA). Input voltage across the matching network was 2 V. Simulated and scanned profiles are shown in Figure 7.3. Length of the focus along a line at 45° to *X-axis* were 12 mm and 10.5 mm

in simulated and scanned pressure profiles while Length of the focus along a line at 135° to *X-axis* were 12 mm and 10.7 mm in simulated and scanned pressure profiles. The farthest dimension of -6 dB contour along X and Y axis in scanned pressure profile was 11 mm. Further, we measured the highest pressure in the focal plane with an optical hydrophone (Model FOPH 2000, RP Acoustics, Leutenbach, Germany). The highest input voltage across the matching network was 388 V (peak-to-peak) and voltage across the elements was 2630 V (peak-to-peak). The Highest positive pressure amplitude was 7.15 MPa while the lowest negative pressure amplitude was -4.9 MPa. Figure 7.4 shows pressure amplitude values at focus for an input voltage from power supply.

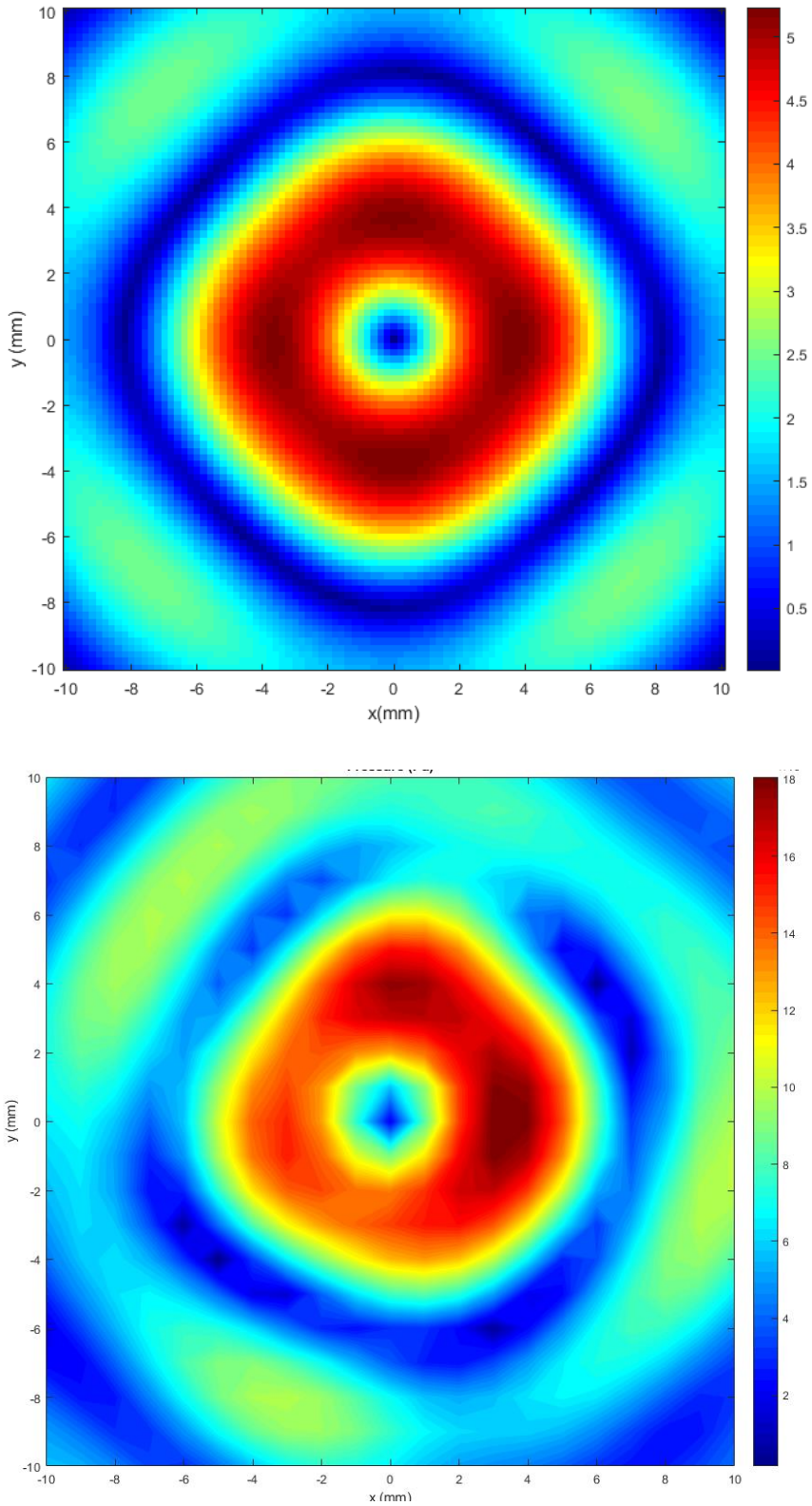

Figure 7.3 Focal plane of the transducer was scanned to confirm shape of the beam. Top image shows simulated pressure profile while the bottom one shows scanned pressure profile.

Length of the focus along a line at 45° to X-axis are 12 mm and 10.5 mm in simulated and scanned pressure profiles. Length of the focus along a line at 135° to X-axis are 12 mm and 10.7 mm in simulated and scanned pressure profiles. Farthest dimension of -6 dB contour along X and Y axis in scanned pressure profile is 11 mm.

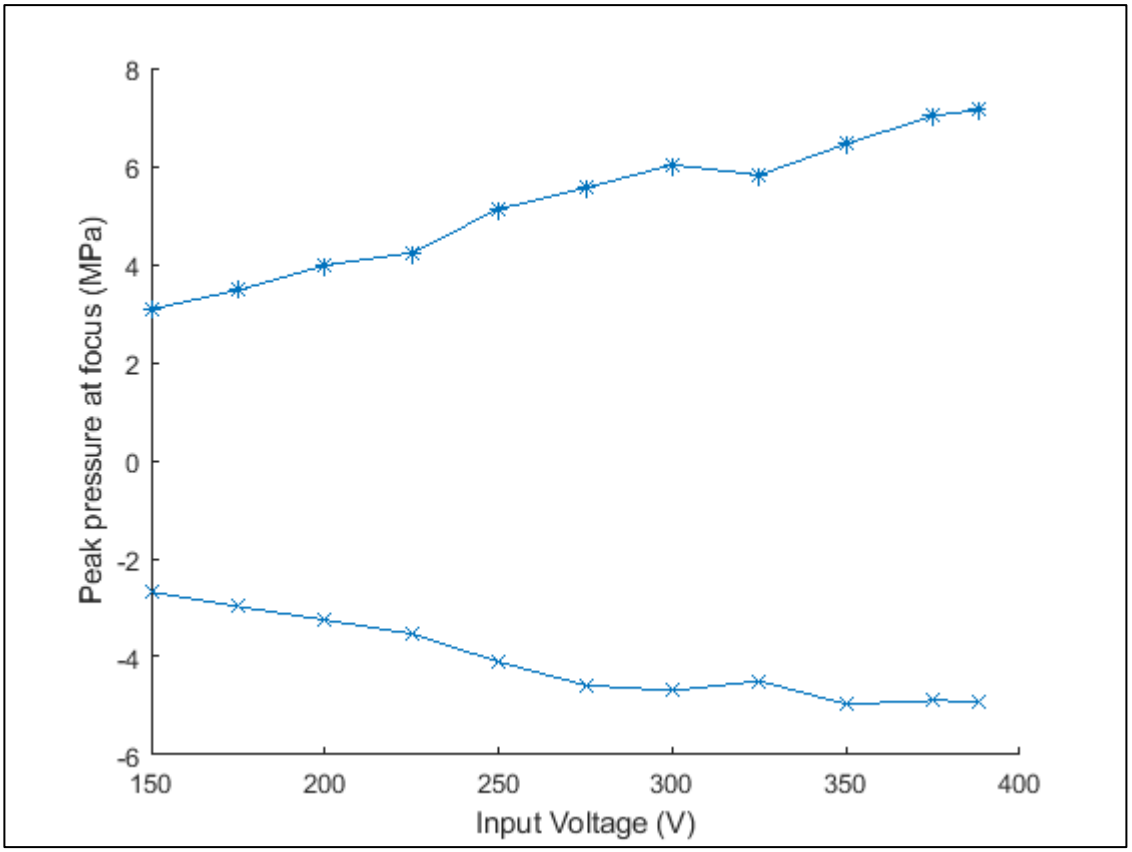

Figure 7.4 The amplitude of pressure produced by the broadly focused transducer was measured at (3 mm, 0 mm) in the focal plane shown in Figure 7.3. As we increase voltage of power supply from 150 V to 388 V across the matching network, voltage across each element increased from 1090 V to 2630 V resulting in increasing pressure amplitude at the focus. Highest positive amplitude was 7.15 MPa while lowest negative amplitude was -4.9 MPa.

7.2 Fragmentations of large stones with the broadly focused transducer

An experiment was designed to study if the transducer fragmented large stones efficiently. Artificial stones made from Begostone Plus plaster (Bego USA, Lincoln, RI), were formed into cylinders with dimensions: 11 mm length X 6 mm diameter (avg. weight = 690 mg). The powder was mixed with water in ratio 4:1 by weight and stones were soaked until the experiment. Liu et al. have demonstrated the artificial stones made from Begostone Plus plaster have mechanical properties similar to natural stones and can be used as stone phantoms.[1], [2] The broadly focused transducer was set up in a water tank similar to the setup in Ch. 2. Water in the tank was degassed to maintain a gas concentration below 30% of the saturation level of dissolved oxygen (Oxi 330i meter with a CellOx 325 probe, WTW, Weilheim, Germany). The stones were fragmented with the broadly focused transducer and a perfectly focused transducer which had focal width of 6 mm. Both transducers were operated at 350 kHz with pulse repetition frequency of 20 and same negative pressure amplitude (-4.9 MPa) for 30 minutes. While fragmenting stones with the transducer having enlarged focus, it was expected to produce more dust as compared to narrow focused transducer. Hence, stones were fragmented in a wire basket studied in Ch. 2. This arrangement mitigated effects of dust during fragmentation. Weight of fragments larger than 2 mm was measured every 10 minutes.

The results are shown in Figure 7.5. The broadly focused transducer fragmented 44 ± 9 % of stone by weight in 30 minutes whereas the focused transducer fragmented only 16 ± 4 % of the stone in the same duration. Rate of fragmentation with broadly focused transducer and focused beam transducer were 9.9 ± 2.0 mg/min and 3.6 ± 0.9 mg/min respectively. However, the rate of fragmentation varied over time. For the broadly focused transducer, the average rate of fragmentation was 7.9 ± 1.7 mg/min in the first 10 minutes and 11.4 ± 2.6 mg/min in the last 10

minutes. The rate didn't change significantly for focused transducer. It increased from 3.1 ± 0.4 mg/min to 4.1 ± 0.9 mg/min for the same time windows.

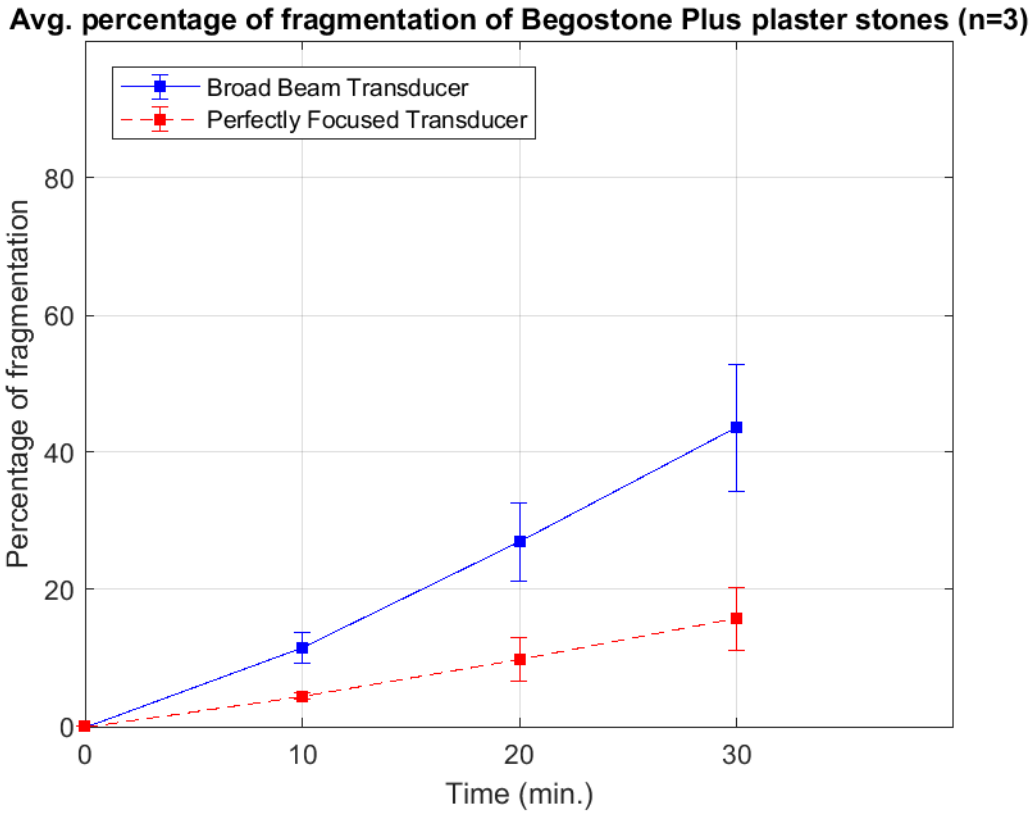

Figure 7.5 Artificial plaster stones which mimic human stones were fragmented with the broadly focused transducer (focal width ~ 11 mm) and perfectly focused transducer (focal width = 6 mm). The cylindrical stones had diameter of 6 mm and length of 11 mm. They were fragmented for half an hour and weight of fragments smaller than 2 mm was measured every 10 minutes. The transducers were operated at 350 kHz with pulse repetition frequency of 20 and at same negative pressure amplitude (-4.9 MPa). The broadly focused transducer fragmented 44 ± 9 % of stone by weight in 30 minutes whereas the focused transducer fragmented only 16 ± 4 % of the stone in the same duration.

7.3 Discussion

The broadly focused transducer was designed with lens developed in Ch. 6 and PZT material tested in Ch. 4. The transducer was fabricated and characterize to confirm the pressure field. The pressure profile in the focal plane closely matched with simulated pressure profile with a few distortions. The size of the -6 dB contour was smaller than that of the simulated pressure profile and the measure pressure profile in section 6.3 with single element transducer. The most important difference in the designs of the transducers used in section 6.3 and section 7.1.5 was how PZT elements were designed. The BWL transducer in section 7.1.5 has four elements powered separately. The radiating area lost in supporting structures these elements might be shrinkage of the -6 dB contours. As mentioned earlier in section 6.4, the distortions may be attributed to the fact that the shape in the focal plane was not symmetric about axis of the transducer in the direction of propagation and the region near the axis had higher focal gain. Although the highest positive pressure amplitude produced by the transducer was about 7 MPa, the lowest negative pressure amplitude was -4.9 MPa. The difference in the positive and negative amplitude may be due to the cavitation during the negative phase. Although, the cavitation was not noted during the measurements, it was observed on ultrasound imaging during fragmentation of the stones. One of the other possible factors for the difference in amplitudes is sensitivity of the fiber optic hydrophone at such low pressures.

The rate of fragmentation of the stones with broadly focused transducer was higher than the rate of the fragmentation of stones with narrowly focused transducers. Based on the rates of the fragmentation, duration for fragmentation of a stone (avg. weight = 690 mg) can be estimated. If we assume rate of fragmentation same as in the last 10 minutes of fragmentation for rest of the fragmentation, the broadly focused transducer can fragment the stone completely in 64 minutes

whereas the focused beam transducer will fragment the stone in 171 minutes. Hence, the broadly focused transducer can potentially reduce duration of the treatment by an estimated 62%. It should be noted that the length of the stones was 11 mm and the stones were placed in the basket such that the stones completely fit within the focus of the broadly focused transducer. Further, the diameter of the stones was 6 mm and rate of the fragmentation might had been different if spherical stones with 11 mm diameter were used.

Future work can be focused on fabricating transducer which can generate negative pressure amplitude up to -6.5 MPa. Further, the lens can be modified to avoid uneven distribution pressure with the focus. One of the ways to ensure effective focusing could be designing arrangement of elements in concave shaped housing. Further, the holographic lenses can be developed for other HIFU applications such as treatment of kidney cancer.

7.4 Conclusion

Using the described rapid prototyping method and a holographic lens designed in Ch. 6, a transducer was fabricated and characterized. Inner diameter, outer diameter, focal distance, frequency of the transducer were 80 mm, 40 mm, 84 mm and 335 kHz respectively. The transducer produced annular shaped pressure profile with focal width of 11 mm and maximum negative amplitude of focal pressure was -4.9 MPa. This focal width was 5 mm larger than the focus produced by perfectly focused transducer for given design constraints. Hence, the broadly focused transducer was supposed to break stones up to 11 mm effectively as opposed to the perfectly focused transducer which breaks stones effectively up to 6 mm. Plaster stones with diameter 6 mm and length 11 mm were fragmented at -4.9 MPa and pulse repetition frequency of 20 with the broadly focused transducer and focused transducers. The broadly focused transducer fragmented

44 ± 9 % of a stone by weight in 30 minutes whereas the focused transducer fragmented only 16 ± 4 % of a stone in the same duration. Based on the observations of the rate of fragmentation, broadly focused transducer and focused beam transducer can fragment the stone completely in 64 minutes and 171 minutes respectively. Thus, the broadly focused transducer can reduce treatment time substantially.

References:

[1] Y. Liu and P. Zhong, "BegoStone—a new stone phantom for shock wave lithotripsy research (L)," *J. Acoust. Soc. Am.*, vol. 112, no. 4, pp. 1265–1268, Oct. 2002.

[2] E. Esch, W. N. Simmons, G. Sankin, H. F. Cocks, G. M. Preminger, and P. Zhong, "A simple method for fabricating artificial kidney stones of different physical properties," *Urol. Res.*, vol. 38, no. 4, pp. 315–319, Aug. 2010.

Appendix A **Surface pressure output of PZ36**

Following table summarizes results of tests of a PZ36 element with matching layer and lens material. Impedance of the element was 20 ohms and it was operated at 350 kHz. Pulse repetition frequency was varied between 500 and 20 to avoid heating in the element but to ensure enough radiation force to measure on weight scale.

Power Supply Voltage (V)	Peak-to-peak voltage across elements (V)	Acoustic power (W)	Electric power (W)	Acoustic Intensity (kW/m^2)	Electric Intensity (kW/m^2)	Surface Pressure amplitude (MPa)	Efficiency
50	480	13.67	21.36	21.87	34.18	0.26	0.64
60	580	19.16	31.14	30.65	49.82	0.30	0.62
70	670	26.80	42.57	42.89	68.11	0.36	0.63
80	770	34.17	56.22	54.68	89.95	0.40	0.61
90	847	44.21	72.33	70.73	115.72	0.46	0.61
100	922	54.91	88.58	87.85	141.72	0.51	0.62
110	1090	64.90	116.52	103.85	186.44	0.56	0.56
120	1173	74.20	138.27	118.73	221.23	0.59	0.54
130	1273	85.92	161.83	137.47	258.93	0.64	0.53
140	1370	101.54	186.45	162.47	298.31	0.70	0.54
150	1477	114.75	215.97	183.59	345.56	0.74	0.53
160	1567	132.97	242.03	212.75	387.25	0.80	0.55
170	1643	154.17	270.02	246.68	432.03	0.86	0.57
180	1743	181.88	301.78	291.01	482.84	0.93	0.60

210	2030	224.10	398.82	358.56	638.11	1.03	0.56
220	2127	235.72	437.11	377.15	699.38	1.06	0.54
230	2213	247.81	475.21	396.50	760.34	1.09	0.52
260	2460	318.48	625.25	509.57	1000.41	1.23	0.51
270	2540	341.73	670.45	546.76	1072.72	1.28	0.51
280	2630	367.30	717.53	587.68	1148.04	1.32	0.51
290	2700	368.46	766.91	589.54	1227.06	1.33	0.48
300	2770	371.95	811.77	595.11	1298.84	1.33	0.46
310	2850	435.88	901.99	697.40	1443.19	1.44	0.48
320	2917	447.50	956.88	716.00	1531.01	1.46	0.47